SEMMELWEIS EGYETEM

DOKTORI ISKOLA

Ph.D. értekezések

3485.

ZÁVOTI OLIVÉR

Celluláris és molekuláris élettan

című program

Programvezető: Dr. Hunyady László, egyetemi tanár

Témavezető: Dr. Csanády László, egyetemi tanár

FUNCTIONAL ANALYSIS OF COMMON AND RARE CYSTIC FIBROSIS-CAUSING MUTATIONS

PhD thesis

Olivér Závoti

Semmelweis University Doctoral College
Molecular Medicine Division

Supervisor:	László Csanády, MD, DSc
Official reviewers:	Gábor Czirják, MD, DSc
	Gábor Tibor Szántó, PhD
Complex Examination:	
Head:	Péter Várnai, MD, DSc
Members:	László Homolya, DSc
	Gergely Szakács, MD, PhD

Budapest
2026

Table of Contents

List of Abbreviations

ABC	ATP-binding cassette
ADP	adenosine-5'-O-diphosphate
ATP	adenosine-5'-O-triphosphate
cAMP	3',5'-cyclic adenosine monophosphate
CF	cystic fibrosis
CFTR	cystic fibrosis transmembrane conductance regulator
cryo-EM	cryo-electron microscopy
ER	endoplasmic reticulum
ERAD	endoplasmic-reticulum-associated degradation
ETI	elexacaftor-tezacaftor-ivacaftor
NBD	nucleotide-binding domain
NMDG	N-methyl-d-glucamine
P-ATP	N^6-(2-Phenylethyl)adenosine-5'-O-triphosphate
P-dATP	2-deoxy-N^6-(2-phenylethyl)adenosine-5'-O-triphosphate
P_i	inorganic phosphate
PKA	protein kinase A (cAMP-dependent protein kinase)
PKI	PKA inhibitory peptide
P_o	open probability
T_b	mean burst duration
T_{ib}	mean interburst duration
TMD	transmembrane domain
VTD	vanzacaftor-tezacaftor-deutivacaftor

1. Introduction

During my doctoral studies, I investigated the function of both common and rare pathogenic mutations in the Cystic Fibrosis Transmembrane Conductance Regulator (CFTR) anion channel and their responses to current therapeutic regimens. In this introduction, I intend to delineate the most essential background information on this protein and the disease that its pathogenic variants can cause.

1.1. Cystic fibrosis as a disorder of transepithelial anion transport

Cystic fibrosis (CF) is an autosomal recessive genetic disease caused by pathogenic variations in the gene encoding the CFTR protein. It is among the most prevalent life-limiting inherited disorders in populations of European descent and affects approximately 100,000 individuals globally [1-3]. CF is characterised by chronic epithelial dysfunction in multiple organs, including the airways, gastrointestinal tract, pancreas, liver, and reproductive system, reflecting the widespread physiological role of CFTR in epithelial ion and fluid transport [4].

The fundamental defect in CF is impaired transepithelial movement of chloride and bicarbonate ions, which leads to reduced water secretion onto epithelial surfaces [5]. In the respiratory tract, this defect results in dehydration of the airway surface liquid, increased mucus viscosity, and compromised mucociliary clearance. These changes predispose patients to persistent bacterial infection, excessive inflammation, and progressive structural lung damage. Similar disturbances in epithelial hydration and luminal pH underlie pancreatic insufficiency, intestinal obstruction, biliary disease, and infertility. Thus, CF pathophysiology is best understood as a consequence of disrupted epithelial homeostasis caused by insufficient CFTR function. In the sweat duct, however, the reabsorption of chloride ions is deficient, causing a particularly salty sweat; the measurement of sweat chloride concentration was considered for a long time the gold standard of the diagnosis of CF in newborns [6, 7].

1.2. The CFTR anion channel: structure and gating mechanism

CFTR is an anion channel localised to the apical membrane of epithelial cells [8, 9]. Although it belongs to the ATP-binding cassette (ABC) transporter family (ABCC7), it

uniquely functions as an ion channel rather than a transporter. The monomeric protein contains the typical structural components of ABC transporters; it consists of two transmembrane domains (TMD1 and TMD2) that form the ion conduction pathway, two cytoplasmic nucleotide binding domains (NBD1 and NBD2), but it also exhibits a unique, unstructured regulatory (R) domain [10].

CFTR activity requires phosphorylation of the R domain by protein kinase A (PKA). Structurally, PKA exists as an inactive tetrameric holoenzyme composed of two regulatory (R) subunits and two catalytic (C) subunits. In the absence of 3',5'-cyclic adenosine monophosphate (cAMP), the regulatory subunits bind to and inhibit the catalytic subunits. Upon an increase in intracellular cAMP levels – typically generated by adenylyl cyclases following G protein-coupled receptor activation – cAMP binds to the regulatory subunits, inducing a conformational change that releases the active catalytic subunits. These catalytic subunits then phosphorylate serine and threonine residues on target proteins, thereby modulating their activity. Hereafter, I will refer to the free purified catalytic subunit as PKA [11].

PKA-mediated phosphorylation of CFTR is referred to as catalytic activation [12, 13]. In the absence of phosphorylation, the R domain constrains the channel in a closed, inactive conformation as it is wedged between the two NBDs, preventing their dimerisation (Figure 1A, state 1) [14]. Infrequently, when the R domain is in its "released" conformation (Figure 1A, state 2) [14], PKA can bind and phosphorylate the channel. The phosphorylation of multiple serine residues in the R domain induces conformational changes that shift the conformational equilibrium of the R domain towards the "released" state (Fig. 1A, state 5), thereby permitting the binding of adenosine-5'-O-triphosphate (ATP) and the subsequent dimerisation of the NBDs [15].

In addition to phosphorylation, the direct binding of PKA to CFTR can further enhance channel activity by increasing open probability through a rapidly reversible mechanism (Figure 1A, states 3 and 4) [16]. This type of reversible, noncatalytic activation depends on membrane anchoring of PKA via its retractable N-terminal myristoyl group (Fig. 1A, purple zigzag) and can be inhibited by the PKA inhibitory peptide PKI(6-22) [13]. Cryo-electron microscopy (cryo-EM) structures of the open CFTR channel in complex with PKA reveal that the kinase (Fig. 1B, orange surface) binds in the cleft between

NBD1 and the “lasso motif” of TMD1. In this arrangement, a C-terminal ~30-residue segment of the R domain (residues 806-833; Fig. 1B, red surface) extends toward the kinase and docks onto the outer surface of NBD1 and the NBD1-TMD interface. Mapping the structure of PKI(6-22) onto this complex shows that its N-terminal helix (Fig. 1B, dark purple mesh) sterically clashes with the docked R domain segment, indicating that R-domain docking is a critical feature of the reversibly activated state [12].

Channel gating is driven by a cycle of ATP binding and hydrolysis at the NBDs. ATP binding to both NBDs causes formation of a tight NBD1-NBD2 dimer, glued together by two molecules of ATP. In the dimer, both ATP molecules are occluded in composite interfacial binding sites, formed by the Walker A and B motifs of one NBD and the ABC signature sequence of the other [15]. Site 1, flanked by the Walker motifs of NBD1 and the signature sequence in NBD2, is catalytically inactive [17, 18], whereas hydrolysis of the □-phosphate of the ATP bound between the signature sequence of NBD1 and the Walker motifs of NBD2 (Site 2) causes loosening of the dimer interface around Site 2, allowing dissociation of adenosine-5'-O-diphosphate (ADP) and inorganic phosphate (P_i) and binding of a new ATP molecule to initiate a new cycle. These ATP-driven conformational transitions are transmitted to the transmembrane domains, where they control opening and closing ("gating") of the anion permeation pathway. Upon activation by PKA, CFTR channel gating exhibits a bursting pattern: bursts of openings interrupted by brief (~10 ms) "flickery" closures are flanked by long (~1 s) interburst closures. Burst-interburst transitions are linked to the NBD catalytic cycle: ATP binding-induced tight NBD dimerisation initiates a burst of openings; loosening of the NBD dimer interface following ATP hydrolysis terminates the burst [19]. The enzymatically inactive Site 1 can remain dimerised through multiple gating cycles at Site 2 [20-22].

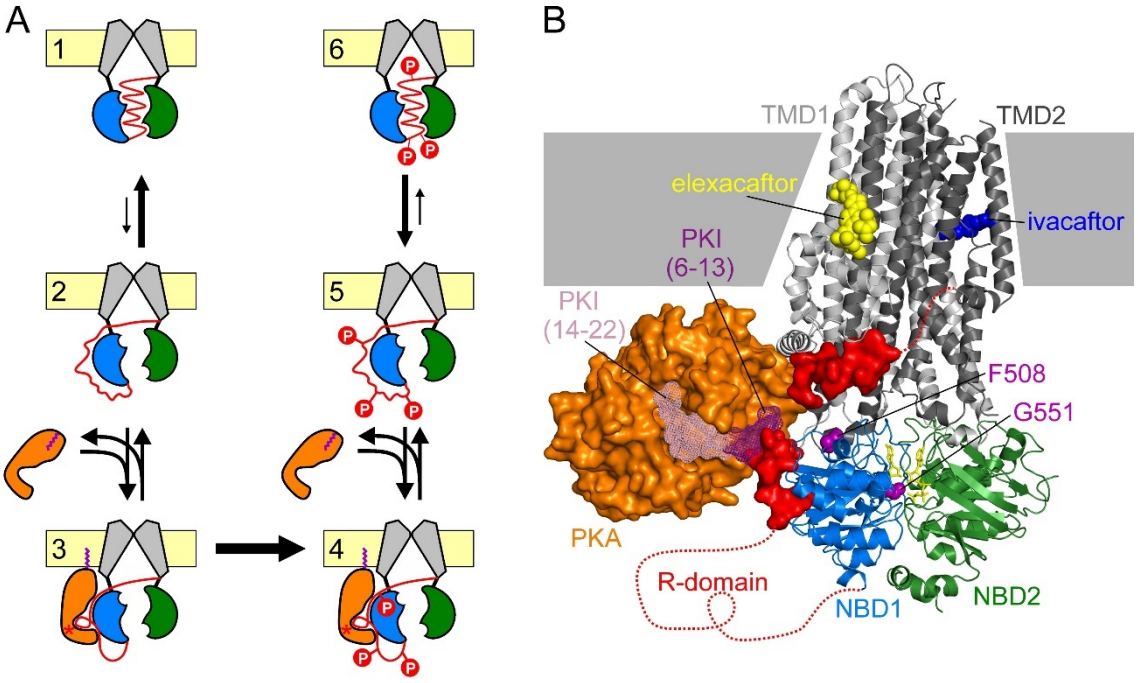

Fig. 1. CFTR gating mechanism and molecular structure. *(A) Kinetic model of CFTR channel regulation by its R domain and PKA. CFTR TMDs, grey; NBD1, blue; NBD2, green; R domain, red ribbon; membrane, yellow; PKA, orange; catalytic site, red asterisk; myristoyl group, purple zigzag. States 2-5 allow channel gating in the presence of ATP (or P-ATP). (B) Cryo-EM structure of the complex of PKA with phosphorylated open (E1371Q) CFTR in the presence of ATP (PDBID: 9dw9). Colour coding is the same as in A. The structure of PKI(6-22) and the drugs elexacaftor and ivacaftor were mapped onto the complex based on PDB structures 2gfc and 8eiq, respectively. ATP bound to NBDs, yellow sticks. Residues F508 and G551 (purple) are shown as purple spheres. Red dotted lines represent unresolved R-domain segments 636-805 and 834-845 and are not drawn to scale.*

1.3. Pathogenic CFTR mutations and functional consequences

The total CFTR-mediated current in a cell (I_{CFTR}) can be calculated as the product of the number of channels at the cell surface (N), open probability (P_o), and single-channel current amplitude (i). Disease-causing mutations in CFTR reduce transepithelial anion fluxes by decreasing the number of channels at the cell surface, impairing channel gating, or limiting ion flow through the pore.

CFTR mutations are commonly categorised into six functional classes based on their dominant molecular defect [23-25] (Fig. 2). Class I mutations result in defective protein synthesis, leading to little or no CFTR production, typically due to nonsense, frameshift, or severe splicing mutations. Class II mutations cause abnormal protein folding and processing, leading to retention in the endoplasmic reticulum (ER) and early proteasomal degradation. Class III mutations produce CFTR proteins that reach the plasma membrane but exhibit defective channel gating. Class IV mutations reduce chloride conductance through the CFTR channel despite proper localisation at the cell surface. Class V mutations lead to reduced amounts of otherwise functional CFTR protein, often due to decreased transcription or abnormal splicing. Class VI mutations are characterised by decreased stability of CFTR at the cell surface, resulting in accelerated turnover and reduced channel abundance. Most mutations belong to Classes I-IV. Although this classification is conceptually useful, many mutations, particularly the most common ones, exhibit multiple defects spanning more than one class.

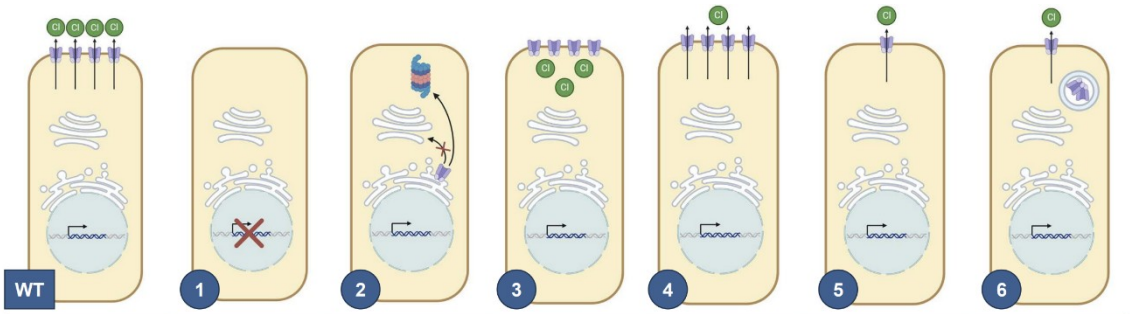

	Class I	Class II	Class III	Class IV	Class V	Class VI
Defect	synthesis	trafficking	gating	conductance	less protein	less stability
Example	G542X	ΔF508	G551D	R117H	A455E	Q1412X

Figure 2. Classification of pathogenic CFTR mutations (based on the work of Lopes-Pacheco, 2016 [26]). *Class I mutations abolish synthesis of the full-length protein; class II mutations disrupt folding and intracellular trafficking; class III mutations impair channel gating; class IV mutations reduce anion permeation through the pore; class V mutations cause reduced protein synthesis; and class VI mutations lead to decreased protein stability.*

1.4. The ΔF508 and G551D mutations

Although more than 2000 pathogenic mutations have been identified, the deletion of phenylalanine at position 508 (ΔF508 or F508del) is the most prevalent CF-causing mutation worldwide, which accounts for approximately 70% of all mutant alleles [3]. This mutation primarily destabilises NBD1 and disrupts its interactions with the TMDs, leading to severe folding defects and subsequently early breakdown through the Endoplasmic Reticulum-Associated Degradation (ERAD) and thus inefficient trafficking to the cell surface [27, 28]. In addition to its processing defect, the small amount of ΔF508 CFTR that reaches the plasma membrane displays impaired gating and reduced stability [29, 30]. Therefore, ΔF508 combines features of Classes II, III, and VI. From a functional perspective, gating of ΔF508 CFTR channels remains tightly linked to NBD dimerisation for channel opening and to ATP hydrolysis for channel closure. Disruption of ATP hydrolysis at Site 2 markedly prolongs channel bursts [31, 32]. The mutation substantially reduces the opening rate by destabilising the transition state for openings [30], a conformation that strains the NBD-TMD interface [33].

Mutation G551D, the third most common CF-causing mutation [34], is an example of a Class III mutation that heavily affects channel gating [35, 36]. Channels bearing this mutation are properly synthesised, folded, and delivered to the cell surface [28] but exhibit extremely low open probability. The substitution interferes with ATP-dependent NBD dimerisation, preventing efficient channel opening despite normal phosphorylation of the R domain. Residue G551 lies within the signature sequence of NBD1, and in the G551D mutant, the negatively charged, non-native aspartate side chain electrostatically repels the γ-phosphate of ATP bound at Site 2. As a result, in G551D CFTR channels, ATP binding at Site 1 stabilises the NBD dimer interface, whereas ATP binding at Site 2 has a destabilising effect [37]. It remains uncertain whether channel opening in this mutant is coupled to NBD dimerisation at Site 2, but the presence of low but detectable ATPase activity in G551D CFTR suggests that formation of a tightly associated dimer may still occur [35].

While most functional studies of the ΔF508 and G551D mutants have concentrated on elucidating how these mutations alter the ATP-dependent gating cycle, some articles

have also indicated that both ΔF508 [38, 39] and G551D [40-42] CFTR exhibit defects in PKA-dependent activation.

1.5. CFTR modulator drugs: mechanisms of action and binding sites

In the past, the average life expectancy of patients with cystic fibrosis was severely reduced due to the absence of therapies targeting the underlying cause of the disease. Treatment was limited to symptomatic management, primarily aimed at alleviating complications rather than correcting channel dysfunction. Clinical care focused on preserving lung function through airway clearance, antibiotics to control recurrent respiratory infections, and supportive measures for pancreatic insufficiency and malnutrition. Progressive lung disease, driven by chronic infection and inflammation, was the leading cause of morbidity and mortality, with recurrent pneumonia representing the most common cause of death in adulthood.

The introduction of highly efficient CFTR modulator drugs that directly target the defective CFTR protein has fundamentally transformed the treatment landscape of CF. These small molecules, developed by Vertex Pharmaceuticals, are designed to correct specific molecular defects in CFTR biogenesis and function and are broadly divided into potentiators and correctors.

1.5.1. Potentiators

Potentiator drugs enhance channel gating. Ivacaftor (VX-770) is the archetypal CFTR potentiator. It increases channel open probability by stabilising the open conformation of the pore. Structural and functional studies indicate that ivacaftor, a highly lipophilic drug, binds to the lipid-exposed outer surface of the transmembrane region of CFTR, near the channel gate [27]. The binding of ivacaftor enhances channel activity independently of ATP binding, by accelerating pore opening and slowing pore closure [43]. This mechanism is particularly effective for gating mutations such as G551D but also improves the residual activity of corrected ΔF508-CFTR.

Deutivacaftor, used in the newest triple combination of CFTR modulators, is a deuterated analogue of ivacaftor with slower metabolic breakdown, providing more stable systemic exposure while retaining the same mechanism of action.

1.5.2. Correctors

Corrector-type drugs improve folding, assembly, and trafficking of mutant CFTR channels. Tezacaftor (VX-661) and elexacaftor (VX-445) bind to distinct sites within the transmembrane domains and exert complementary stabilising effects [44]. Tezacaftor, a type I corrector, primarily stabilises early folding intermediates of TMD1 and its interface with NBD1, thereby enhancing maturation and ER exit. Elexacaftor, a more recently developed type III corrector, has a broader mechanism, stabilising multiple interdomain contacts and improving folding efficiency of ΔF508 CFTR at the plasma membrane. Importantly, elexacaftor also exhibits modest potentiator-like activity, further increasing open probability of corrected channels [45-47]. By targeting multiple folding bottlenecks, the combination of two structurally and mechanistically distinct correctors allows more effective rescue of ΔF508-CFTR than either compound alone [48]. Recently, vanzacaftor, a next-generation corrector, has begun to replace elexacaftor in newer combination therapies.

1.5.3. Triple-combination therapies: ETI and VTD

The combination of elexacaftor, tezacaftor, and ivacaftor (ETI) produces a synergistic increase in CFTR surface expression and channel activity and has demonstrated substantial clinical benefit in patients that carry at least one ΔF508 allele. ETI improves cellular processing, trafficking, and gating of mutant CFTR, leading to higher levels of CFTR protein at the apical membrane and enhanced chloride transport compared with correctors or potentiators alone. Pivotal clinical studies have shown significant improvements in lung function, quality of life, sweat chloride, and other key clinical endpoints in people with CF with one or two copies of the ΔF508 mutation [49]. ETI has been approved by the US Food and Drug Administration (FDA) and the European Medicines Agency (EMA) for the treatment of CF in patients carrying at least one ΔF508 allele. Although G551D is a pure gating mutation, the drug combination is also available for treating this variant. The label has been progressively expanded to include an increasing number of rare alleles.

More recently, vanzacaftor-tezacaftor-deutivacaftor (VTD) has been developed as a next-generation triple therapy. In this combination, vanzacaftor and tezacaftor act as CFTR correctors targeting processing and trafficking defects of mutant CFTR, while the

improved pharmacokinetic properties of the potentiator deutivacaftor support once-daily dosing and sustained channel activation. In clinical evaluations, this next-generation regimen has shown comparable or superior effects on CFTR function and lung function relative to first-generation triple therapy, while expanding efficient therapy to a broader population of people with CF [50].

1.6. Rare pathogenic mutations of the CFTR channel

According to the Cystic Fibrosis Foundation, 92.3% of the CF population in the USA were eligible for at least one CFTR modulator as of 2023 (*Cystic Fibrosis Foundation. (2024). 2023 patient registry annual data report.*). This proportion continues to increase with the introduction of the VTD combination. Despite the success of CFTR modulators, many rare CFTR variants remain insufficiently characterised, restricting therapeutic access for individuals carrying these mutations. In recent years, five rare CF-causing missense mutations – c.377G>A (p.G126D; legacy: G126D), c.1007T>A (p.I336K; legacy: I336K), c.1394C>T (p.T465I; legacy: T465I), c.1745C>T (p.T582I; legacy: T582I), and c.2951A>T (p.D984V; legacy: D984V) – were detected in the Hungarian CF population [51] (Fig. 3). Although most of these variants (with the exception of D984V) had been previously reported in sequencing studies from diverse populations worldwide [52-62], their effects on CFTR folding, channel gating, and drug responsiveness had not been thoroughly investigated. Consequently, the variants T465I, T582I, and D984V are not currently eligible for any CFTR modulator therapy, due to the lack of either clinical and/or molecular characterisation, highlighting the need for extensive research on these variants.

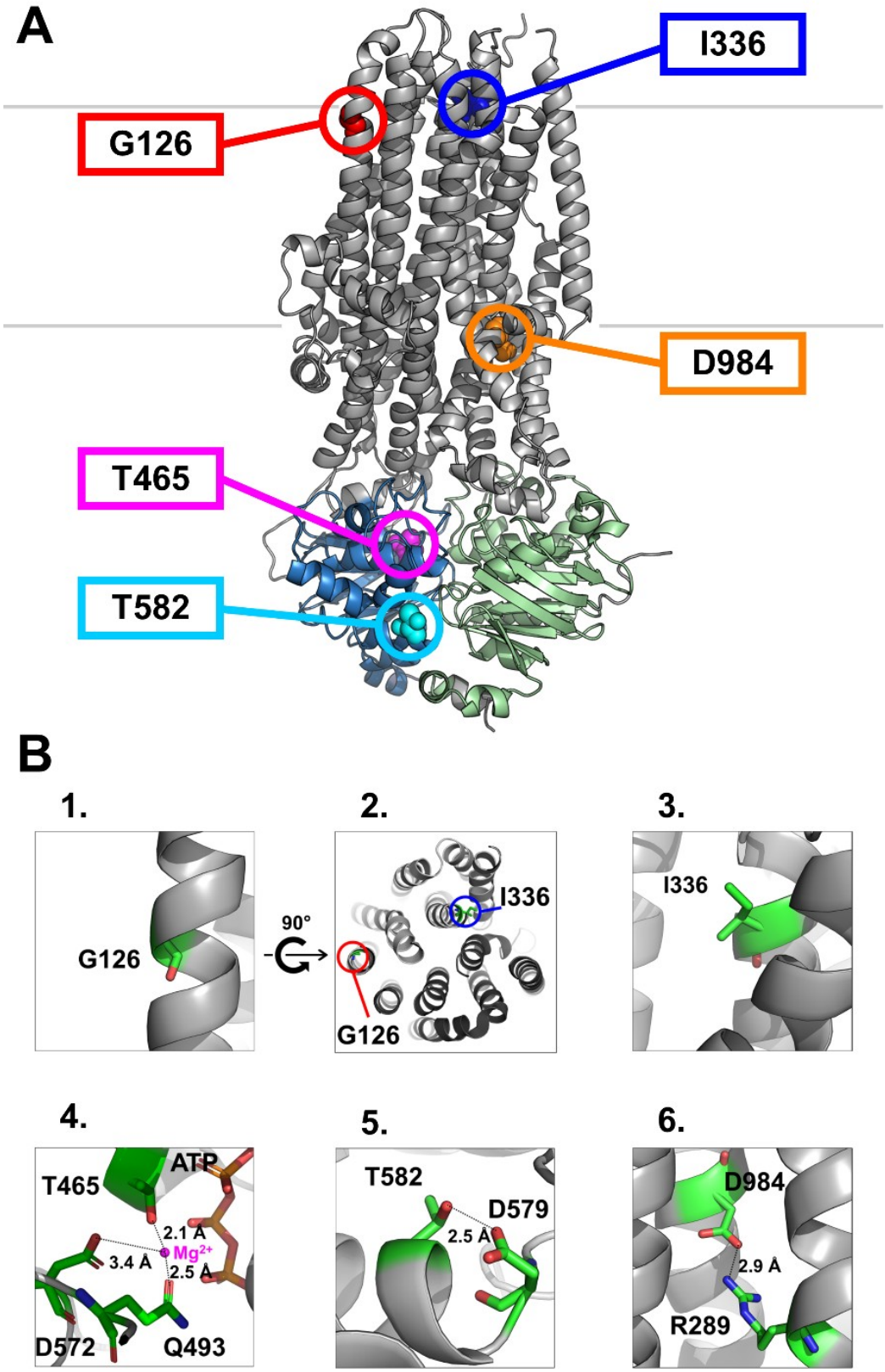
A
I336
G126
D984
T465
T582
B
1.
2.
3.
G126
90°
I336
G126
I336
4.
5.
6.
T465
ATP
2.1 Å
Mg2+
3.4 Å
2.5 Å
D572
Q493
T582
D579
2.5 Å
D984
2.9 Å
R289

Figure 3. Localisation of five rare cystic fibrosis-causing mutations. *(A) The positions of the five CF-causing mutations mapped on the structure of phosphorylated, ATP-bound quasi-open human CFTR (PDB: 6msm). Colour coding: TMDs, grey; NBD1, marine; NBD2, green. Location of the target residues: G126 (red spacefill), transmembrane helix 2 (TM2); I336 (blue spacefill), TM6; T465 (magenta spacefill), NBD1; T582 (cyan spacefill), NBD1; D984 (orange spacefill), TM9. (B) Close-up views of the target residues and their possible interactions. Panels 1-3: The G126 and the I336 side chains are not facing the channel pore. Panel 4: The T465 side chain is the closest of the three side chains that coordinate the* Mg^{2+} *ion in the degenerate site. Panels 5-6: The T582 and D984 side chains might form an H-bond and a salt bridge, respectively, probably involved in stabilising the open-pore structure.*

2. Aims

Cystic fibrosis-causing mutations impair CFTR channel function through diverse mechanisms affecting protein biogenesis, regulation, and gating. The overall aim of this thesis is to define the molecular and functional consequences of both common and rare pathogenic CFTR mutations and to assess their responsiveness to currently available CFTR modulator therapy (ETI).

2.1. Investigating the CFTR-PKA interaction in the ΔF508 and G551D mutants

Although extensive functional studies have focused on the ΔF508 and G551D mutations – particularly their effects on the ATP-dependent gating cycle – evidence also suggests that both mutations exhibit defective PKA-dependent activation. The increasing interest in pharmacological strategies that enhance PKA signalling, including the use of phosphodiesterase inhibitors either alone or in combination with CFTR modulators [63-66], underscores the need for a detailed mechanistic understanding of CFTR-PKA interactions and their modulation by therapeutic compounds. We aim to characterise the defects in PKA-dependent activation of ΔF508 and G551D CFTR by dissecting the reversible and irreversible components of channel activation, and to determine how clinically used CFTR modulators influence PKA-dependent activation and gating behaviour of these mutant channels.

2.2. Assessing the eligibility of rare CF-causing mutations for ETI therapy

By linking structural defects to pharmacological rescue, this work seeks to support the extension of modulator therapies to patients carrying rare CFTR mutations. Recent genetic studies have identified several rare CF-causing missense mutations in the Hungarian CF population, including G126D, I336K, T465I, T582I, and D984V. Although most of these variants have been previously reported in sequencing studies worldwide, their effects on CFTR biogenesis, channel function, and pharmacological responsiveness remain poorly examined. In this study, we evaluate the functional properties of these rare CFTR mutants and their responsiveness to currently available CFTR potentiator and corrector drugs. Addressing these gaps is essential for extending precision-medicine approaches to individuals carrying rare CFTR mutations.

3. Methods

3.1. Ethical approval

Animal experiments were approved by the Semmelweis University Animal Welfare Body (approval number: SEMMAWB/2023-001).

3.2. Molecular biology

All mutations were introduced into the human CFTR/pGEMHE and CFTR/pcDNA3 sequences using the Quick Change II XL Site-Directed Mutagenesis Kit (Agilent Technologies). Plasmid DNA was replicated in *E. coli* (K-12) and purified using the QIAGEN HiSpeed Plasmid Midi Kit. All mutations were confirmed by automated sequencing (LGC Genomics GmbH). The CFTR/pGEMHE plasmids were then linearised using the Nhe I HF restriction endonuclease (New England Biolabs) and transcribed *in vitro* with the mMessage-mMachine T7 Ultra Kit (Agilent Technologies). Purified DNAs and cRNAs were stored at -80°C.

3.2. Expression of CFTR channels in *Xenopus laevis* oocytes

Oocytes were extracted by partial ovariectomy from anesthetised adult female *Xenopus laevis* frogs according to the Institutional Animal Care and Use Committee guidelines and then digested with Collagenase Type II (Gibco). Separated oocytes were stored at 18°C in modified Ringer's solution (82 mM NaCl, 2 mM KCl, 1 mM $MgCl_2$, 5 mM 4-(2-hydroxyethyl)-1-piperazineethanesulfonic acid (HEPES); pH was set to 7.5 with NaOH)) supplemented with 1.8 mM $CaCl_2$ and 50 μg/ml gentamycin. Aliquots of cRNAs of the channel constructs, ranging from 0.1 to 30 ng (in fixed 50 nl volumes), were injected into the oocytes using a Nanoject II injector (Drummond Scientific). Recordings were performed 1-4 days after the injection.

3.3. Inside-out patch clamp recordings

The patch pipette solution contained 138 mM N-methyl-d-glucamine (NMDG), 2 mM $MgCl_2$, 5 mM HEPES (pH was set to 7.4 with HCl). The bath solution contained 138 mM NMDG, 2 mM $MgCl_2$, 5 mM HEPES, 0.5 mM EGTA (pH was set to 7.1 with

HCl). Inside-out membrane patches were excised and transferred to a rapid-exchange flow chamber, allowing solution changes with a time constant of less than 100 ms using ALA-VM8 electronically controlled valves (Ala Scientific Instruments, Farmingdale, NY, USA). All measurements were performed at 25°C. Macroscopic currents were recorded at a membrane potential of −40 mV, single-channel currents at −80 mV, and unitary conductances were obtained from recordings at multiple different membrane potentials ranging from −80 to +40 mV. Amplified currents were low-pass filtered at 1 kHz (Axopatch 200B, Molecular Devices, Sunnyvale, CA, USA), digitised at 10 kHz (Digidata 1550B, Molecular Devices) and recorded to disk (pCLAMP 11, Molecular Devices).

MgATP was prepared by diluting a 400 mM aqueous stocks (adjusted to pH 7.1 with NMDG) into the bath solutions. Potentiators, ivacaftor (VX-770, Selleck Chemicals) and elexacaftor (VX-445, Selleck Chemicals) were diluted from concentrated dimethyl sulfoxide-based stocks (>100x) into the bath solutions. N^6-(2-phenylethyl)adenosine-5′-O-triphosphate (P-ATP, Biolog LSI) and 2-deoxy-N^6-(2-phenylethyl)adenosine-5′-O-triphosphate (P-dATP, Biolog LSI) were freshly dissolved in the bath solution to final concentrations of 10 and 50 μM, respectively. The catalytic subunit of bovine PKA was prepared from beef heart as described [13], and was diluted into the bath solution from 40-60 mM stock solutions. For experiments requiring 1.2 mM PKA (Fig. 8), the ~150 mM potassium phosphate buffer of the PKA stock was exchanged to 10 mM potassium phosphate using a Hi-TRAP desalting column (GE Healthcare). Consequently, the final phosphate concentrations in all recordings remained below ~1 mM.

3.4. Data analysis

Macroscopic raw data traces were Gaussian filtered at 50 or 100 Hz, then the baseline was subtracted. For single-channel kinetic analysis (Figures 10, 14, and 16), recordings from patches containing five or fewer active channels were idealised by half-amplitude threshold crossing. The events lists were fitted with the $C_1 \leftrightarrow O_3 \leftrightarrow C_2$ model using a simultaneous maximum likelihood fit to the dwell-time distributions at all conductance levels, with an imposed fixed dead time of 4 ms [67]. The obtained transition rate constants k_{13}, k_{31}, k_{23} and k_{32} were used to calculate mean burst (T_b) and interburst (T_{ib}) durations as $T_b = (1/k_{31})(1+k_{32}/k_{23})$, and $T_{ib} = 1/k_{13}$. Opening and closing rates were

defined as the rate of entering ($1/T_{ib}$) and exiting ($1/T_b$) a burst, respectively. The open probability (P_o) was calculated from the events lists as $P_o = (\sum_k t_k l_k)/(NT)$, where t_k and l_k indicate the duration and current level, respectively, of the kth event, N is the number of channels in the patch, and T is the total recording time. N was estimated as the maximum number of simultaneously open channels in the patch in the presence of either P-dATP + PKA (for the rare mutants), or ATP + PKA + VX-770 (ivacaftor) + VX-445 (elexacaftor) (for the ΔF508 mutant).

For I336K and T465I, upper bounds for P_o in 2 mM ATP were estimated from the maximal fractional stimulation by drugs (see Fig. 15F, right), using the relationship $P_o \leq I_{ATP}/I_{max}$, where I_{ATP} represents the average current measured in 2 mM ATP, and I_{max} denotes the maximal current observed in the same patch in the presence of P-dATP + PKA + VX-770 (ivacaftor) + VX-445 (elexacaftor). The closing rate ($1/T_b$) in 2 mM ATP was determined by dwell-time analysis, as performed for the other three constructs. An upper bound for the opening rate ($1/T_{ib}$) in 2 mM ATP was then derived from the relationship $P_o \approx T_b/(T_b + T_{ib})$. Accordingly, $(1/T_{ib}) \leq (1/T_b) \cdot I_{ATP}/(I_{max} - I_{ATP})$.

3.5. Channel expression in HEK-293T cells

HEK-293T cells were cultured in T-175 flasks at 37°C in Dulbecco's Modified Eagle's Medium (DMEM) with 4.5 g/l glucose supplemented with 10% fetal bovine serum (FBS), 2 mM l-glutamine, and 100 units/ml penicillin/streptomycin. After reaching ~70-80% cell confluency, the cell cultures were transiently transfected with the CFTR/pcDNA3 constructs using Lipofectamine 3000 Transfection Reagent (Thermo Fisher, Waltham, MA, USA) according to the protocol provided by the manufacturer.

3.6. Crude membrane preparations

After 48 h of incubation following transfection, upon reaching ~100% cell confluency, the cells were washed with ice-cold divalent-free phosphate-buffered saline (PBS), then 1.3 ml Lysis Buffer (10 mM HEPES, 1 mM EDTA, 1 mM phenylmethylsulfonyl fluoride (PMSF), 1 μg/ml leupeptin and 1 μg/ml pepstatin, pH 7.2) was added to each flask. The cells were scraped off the flasks and pipetted into a Dounce homogeniser. After a 5 min incubation on ice, the cells were ruptured with 10 strokes. Then, 325 μl sucrose buffer (1.25 M sucrose, 10 mM HEPES, pH 7.2) was added to the lysate and

mixed with a single stroke. Cell debris was pelleted at 4°C and 3000 g for 10 min. The supernatant was centrifuged at 4°C and 16,000 g for 30 min. The pellet was resuspended with 50 µl of Sample Buffer (62.5 mM Tris-HCl, 3% SDS, 10% glycerol, 0.05% bromophenol-blue, pH 6.8). For the experiments with corrector drugs (Fig. 12), the cell cultures were transfected at ~50-60% cell confluency. Then, 24 h after transfection, 3 µM elexacaftor (VX-445) and 3 µM tezacaftor (VX-661) were added to the media. After an additional 24 h, the cells were ruptured, and crude membrane preparations were made as described above.

3.7. Western blot

Aliquots of 3 µl of the above-described crude membrane preparations were diluted with 7 µl of Sample Buffer. After adding 0.5 µl of 1 mM DTT, the samples were incubated at 65°C for 15 min, loaded onto 7.5% polyacrylamide gels, and separated at a voltage of 80-120 mV. The gels were transferred to nitrocellulose membranes by a 10-minute run on a Bio-Rad Trans Blot Turbo system at 2.5 A and 25 V. Following transfer, the membranes were blocked for 1 h in 5% BSA dissolved in Tris-buffered saline (TBS) supplemented with 0.2% Tween 20 (TBST). Primary antibodies were provided by Dr Martina Gentzsch's laboratory at the University of North Carolina at Chapel Hill through the Cystic Fibrosis Foundation. For our studies, the 5E2 monoclonal antibody, which recognises the C-terminal portion of NBD2 (residues 1371-1385), was used at 1:5000 dilution (in TBST + 0.5% BSA). After overnight incubation with the primary antibody at room temperature, the membranes were washed 3× for 10 min in TBST + 0.5% BSA. Then, alkaline-phosphatase-conjugated anti-mouse secondary antibody was added at a 1:10,000 dilution. After 2 h of incubation, the membranes were washed 3× for 10 min with TBST. The signal was detected by adding 10 ml alkaline phosphatase buffer, made according to the manufacturer's (Roche, Indianapolis, IN, USA) protocol, supplemented with 50 µl of 4-nitroblue tetrazolium chloride (NBT) and 37.5 µl of 5-bromo-4-chloro-3-indoyl phosphate (BCIP) solutions.

3.8. Densitometric analysis

For densitometric analysis, membranes were scanned as 8-bit greyscale images; all pixel densities remained well below 255. Within each lane, pixel densities were then averaged

across rows of pixels and plotted as a function of vertical position, resulting in densitograms for each lane. Following subtraction of the densitogram of the control lane, 'baseline-subtracted' densitograms were fitted with sums of three Gaussian functions, corresponding to the positions of Bands A, B and C. Band A, B and C densities were defined as the areas under the respective Gaussian component. Finally, Band C densities were normalised either to that of wild-type (WT) CFTR on the same blot (Fig. 12C) or to the sum of the densities of the three bands for the respective construct (Fig. 12D).

3.9. Statistics

All data are given as mean ± SD. The number of electrophysiological experiments ('n') shown in the figures indicates the number of excised patches. For each independent biological replicate used for western blots, all six constructs were handled in parallel: cell cultures were passaged, transfected, and lysed simultaneously on the same days. Significance levels were obtained using Student's t-test. The threshold of significance was chosen to be $p < 0.05$.

4. Results

4.1. Interactions of the ΔF508 and G551D mutants and the catalytic subunit of PKA

4.1.1. Increased noncatalytic activation by PKA for both ΔF508 and G551D CFTR in the presence of an ATP analogue

N^6-(2-phenylethyl)-ATP (P-ATP) is a high-affinity ATP analogue that is able to bind to the CFTR protein and drive channel gating [68, 69]; however, P-ATP cannot bind to PKA and thus cannot support phosphorylation [16, 70]. Consequently, noncatalytic (reversible) CFTR activation mediated by PKA binding can be selectively assessed by applying PKA to channels that are gating in the presence of P-ATP [16]. Inside-out membrane patches from *Xenopus laevis* oocytes expressing ΔF508 or G551D CFTR mutants were sequentially exposed for approximately ~1-min intervals to 300 nM PKA under three conditions: in the presence of, first, P-ATP (10 μM), then ATP (2 mM), and finally P-ATP again (Fig. 4). The application of PKA in P-ATP selectively elicited noncatalytic stimulation of non-phosphorylated and phosphorylated channels, respectively. PKA application in ATP induced both catalytic (irreversible) activation, due to phosphorylation, and noncatalytic activation, which manifested as a partial current decline after the removal of PKA (Fig. 4A and B, centre; Fig. 4C and D, second blue arrow) [16]. Notably, in our inside-out patch experimental setting, noncatalytic activation is rapidly reversible upon PKA washout, in contrast to catalytic activation, which is considered irreversible due to the absence of cytosolic phosphatases that dephosphorylate CFTR in intact cells [16].

For both variants, noncatalytic activation by PKA was detectable both prior and following phosphorylation. However, the reversible component of activation of the phosphorylated channels was substantially larger in P-ATP than in ATP (Fig. 4, compare second and third blue double arrows), by more than 2-fold for ΔF508 and by approximately 10-fold for G551D CFTR. Moreover, for ΔF508 CFTR, noncatalytic stimulation of non-phosphorylated channels in P-ATP was approximately 2-fold larger than that observed for phosphorylated channels in ATP (Fig. 4, compare first and

second blue double arrows). These findings contrast with wild-type CFTR, for which the amplitude of the noncatalytic current component is largely independent of whether ATP or P-ATP is used to drive channel gating (Fig. 4, blue double arrows; data replotted from [16]).

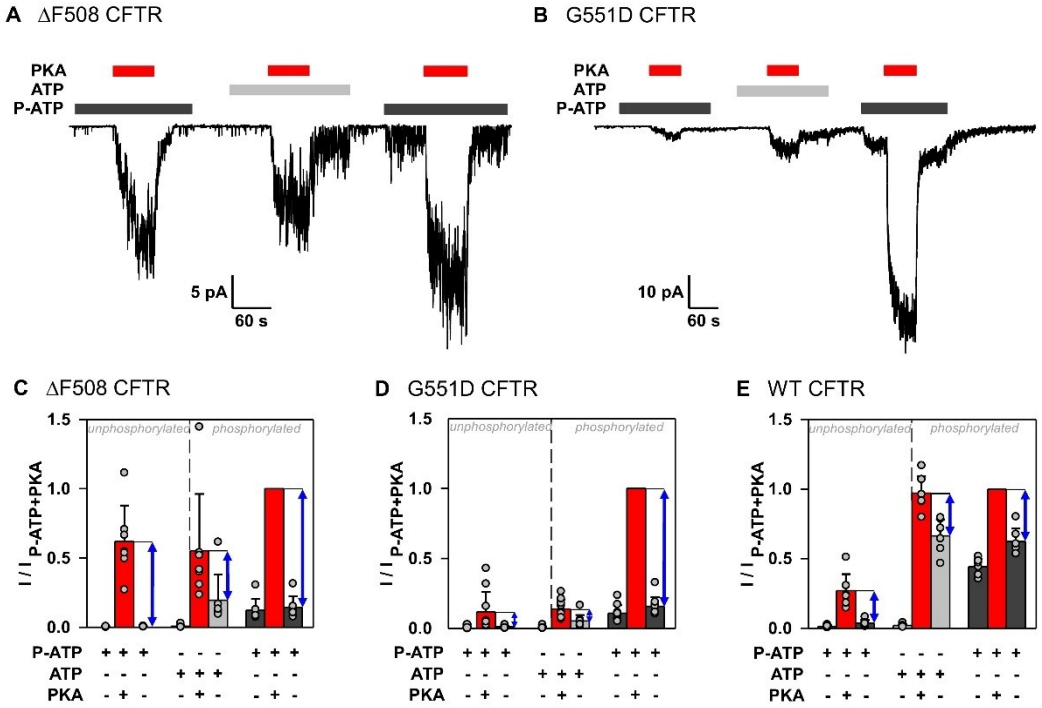

Figure 4. Noncatalytic activation of ΔF508 and G551D CFTR by PKA is enhanced in the presence of P-ATP. *(A-B) Representative recordings from inside-out patches excised from Xenopus laevis oocytes expressing (A) ΔF508 or (B) G551D CFTR. Channel activity was elicited by the application of 10 μM P-ATP (dark grey bars) or 2 mM ATP (light grey bars), in the absence or presence of 300 nM PKA (red bars). Membrane potential was −40 mV; temperature was 25°C. (C-E) Mean steady-state currents measured during the nine consecutive segments of the protocol shown in A-B for ΔF508 (C), G551D (D), and WT (E) CFTR. Currents were normalised to the mean current recorded during the third PKA exposure in the same patch. Data in (E) are replotted from Mihályi et al. [16]) but have been renormalised. Bars represent mean ± S.D. (n = 7 for C; 10 for D; 6 for E). Blue double arrows indicate the magnitude of noncatalytic PKA stimulation for unphosphorylated channels in P-ATP and for (partially) phosphorylated channels in ATP or P-ATP. The ratio of the amplitudes of*

noncatalytic stimulation in P-ATP versus ATP for phosphorylated channels (the ratio of the third to the second blue arrow in C-E), calculated for each patch individually, was 3.39 ± 2.01 (n = 7) for ΔF508, 12.5 ± 5.0 (n = 10) for G551D, and 1.27 ± 0.42 (n = 6) for WT CFTR (mean ± S.D.). This ratio was significantly larger for both mutants than for WT (p = 0.0285 and p = 9.06 × 10⁻⁵, respectively; Student's 2-sample t-test).

4.1.2. Slower activation by PKA for both ΔF508 and G551D CFTR channels

Literature suggests slower activation by PKA of both ΔF508 [39] and G551D [41] CFTR, raising the possibility that the 1-min ATP + PKA exposure used in our protocol shown in Fig. 4A-B may not suffice to achieve complete phosphorylation. To address this, we examined current activation for both mutants over prolonged PKA application (~4 minutes; Fig. 5A, D). Confirming previous findings [39], current activation of ΔF508 CFTR was markedly delayed as the current reached only ~50% of its maximal level after a 1-minute exposure to ATP + PKA (Fig. 5A and G, red bars) in comparison with WT CFTR, for which ~90% of the maximal current develops within one minute (Fig. 5I, red bars; data replotted from Mihályi et al. [13]). As for G551D CFTR, the extended exposure in ATP + PKA (Fig. 5H) did not indicate reduced fractional activation after the first minute. Of note, the small amplitudes and pronounced stochastic fluctuations of G551D currents limit the reliability of this approach.

To estimate the activation half-times of the mutant channels, we constructed macroscopic currents for both mutants by summing currents from eight patches aligned to the onset of PKA application (Fig 5 B, E). Analysis of these summed currents yielded activation half-times ($t_{1/2}$) of ~40 s for ΔF508 and ~29 s for G551D CFTR (Fig. 5B and E; L-bars and black numbers), both of which were substantially prolonged compared to WT CFTR ($t_{1/2}$ = 11.8 ± 1.4 s, n = 13; Fig. 5B and E, blue traces).

Notably, the ratio between reversible (noncatalytic) and irreversible (catalytic) components of activation was also altered in both mutants. For WT CFTR channels exposed to 300 nM PKA, these components contribute approximately equally to the total current (Fig. 5I, right; compare blue double arrow with grey bar). On the other hand, for phosphorylated ΔF508 and G551D CFTR, the total current measured in ATP + PKA was dominated by the reversible component (Fig. 5G-H, right). Macroscopic

currents generated by summing patch currents synchronised to PKA washout (Fig. 5C and F) indicate that, in both mutants, the reversible component accounts for ~75-80% of the total current, whereas the irreversible component contributes only ~20-25%. Therefore, both mutations impair catalytic activation to a greater extent than noncatalytic activation.

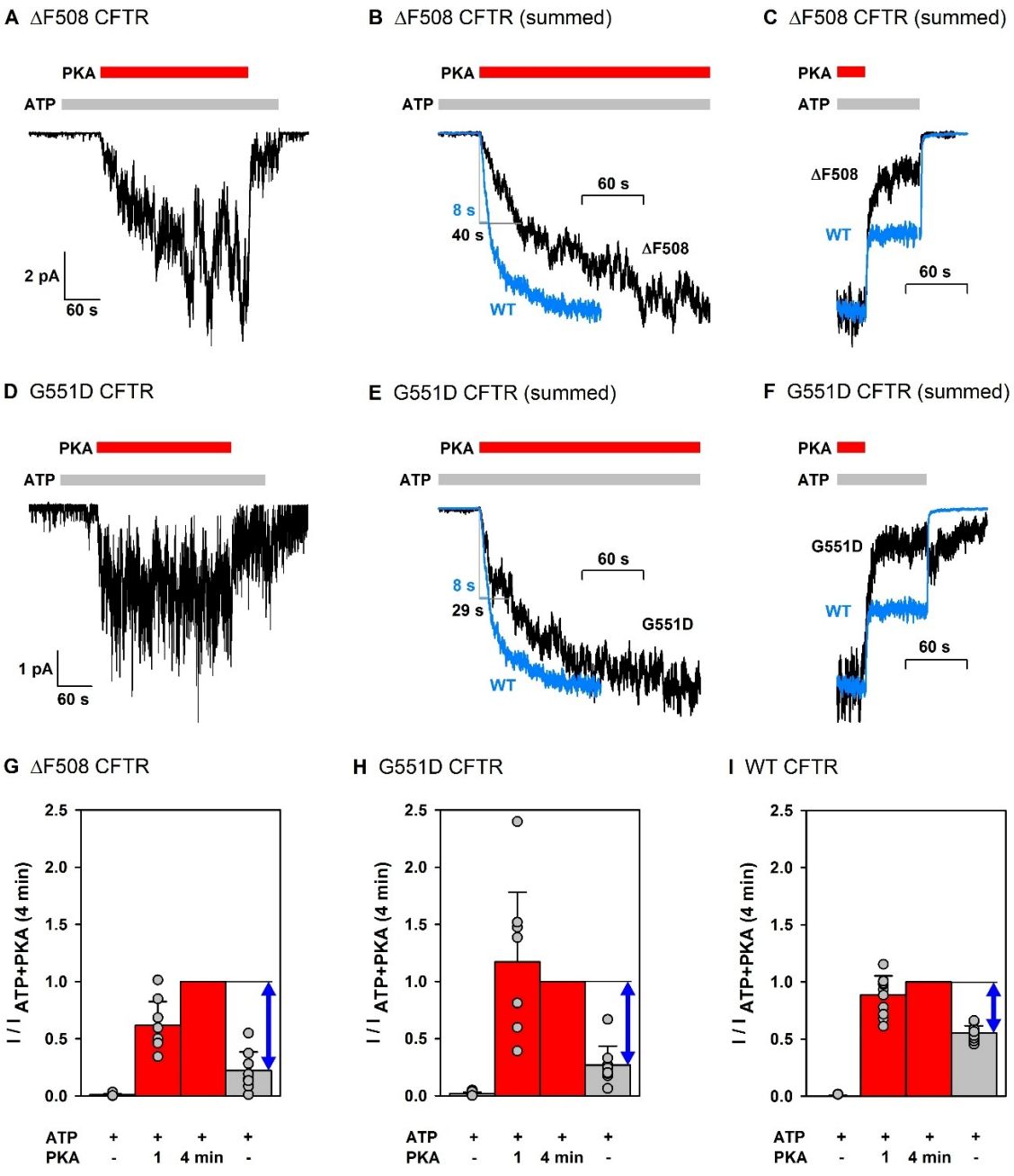

Figure 5. PKA-evoked ΔF508 and G551D CFTR currents develop more slowly than WT and are dominated by noncatalytic activation. *(A, D) Quasi-macroscopic inside-out patch recordings of (A) ΔF508 and (D) G551D CFTR during a 4-minute exposure*

to 300 nM PKA (red bars) in the continuous presence of 2 mM ATP (grey bars). (B, C, E, F) Synthesised macroscopic currents obtained by summing quasi-macroscopic recordings from 6-11 patches. Panels (B, E) show channel activation upon PKA addition, and (C, F) partial deactivation following PKA removal, for (B, C) ΔF508 and (E, F) G551D CFTR. Individual traces were aligned to the time of PKA addition (B, E) or removal (C, F). Overlaid blue traces represent the corresponding time courses from a single representative WT macroscopic trace. All currents were normalised to their maximal amplitudes. In (B, E), L-shaped bars and numbers indicate activation half-times ($t_{1/2}$, in seconds). (G-I) Fractional currents recorded in 2 mM ATP before PKA exposure (first bar), after 1 min (second bar) or 4 min (third bar) of exposure to 300 nM PKA, and after PKA removal (fourth bar) for (G) ΔF508, (H) G551D, and (I) WT CFTR. Currents were normalised to the amplitude measured after 4 minutes in PKA in the same patch. Bars represent mean ± S.D. (n = 8 for G; 8 for H; 11 for I). Blue double arrows indicate the magnitude of noncatalytic PKA stimulation following 4 min of PKA exposure. Data in (I) are replotted from Mihályi et al. [13]. The ratio of the current amplitude in ATP after PKA removal to that in ATP + PKA (Fig. 5G-I, 4th bar) was significantly smaller for both ΔF508 and G551D compared to WT ($p = 1.08 \times 10^{-5}$ and $p = 7.90 \times 10^{-5}$, respectively; Student's 2-sample t-test).

Although the data in Fig. 5B and G suggest that ΔF508 channels did not reach full phosphorylation under the protocol used in Fig. 4A, the marked enhancement of noncatalytic stimulation in the presence of P-ATP was confirmed using longer PKA exposures (>2 min in P-ATP and ~4 min in ATP; Fig. 6A). Because prolonged recordings led to substantial current rundown in some patches, currents measured during the three consecutive segments (P-ATP, ATP, P-ATP) were analysed separately and normalised to the current recorded in the presence of PKA within each respective segment. These experiments again demonstrated a strong enhancement of noncatalytic stimulation of phosphorylated ΔF508 channels by PKA in P-ATP compared with ATP (Fig. 4A, C), as reflected by the larger fractional stimulation (Fig. 6B, right vs centre; ratio of 2nd to 3rd bar). Consistent with the dominance of noncatalytic activation in total ΔF508 channel activity in ATP + PKA (Fig. 5A, G), removal of PKA produced a larger fractional current decrease than observed for WT channels (Fig. 6B vs 6C, centre, 3rd bar).

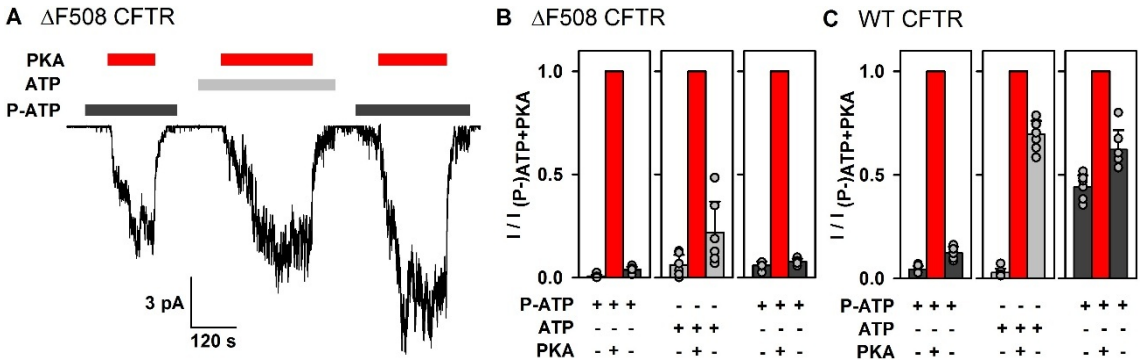

Figure 6. Noncatalytic activation by PKA is further enhanced by P-ATP even in fully phosphorylated ΔF508 CFTR. *(A) Representative current recording from an inside-out patch expressing ΔF508 CFTR using the protocol shown in Fig. 4A, but with prolonged PKA exposures. PKA was applied for >2 minutes in the presence of P-ATP and for ~4 minutes in the presence of ATP. (B) Fractional steady-state currents measured during the nine consecutive segments of the protocol shown in (A). Because substantial current rundown was observed in some patches during the prolonged (~18 min) recordings, currents in the three consecutive sections (P-ATP, ATP, P-ATP) are presented separately, each normalised to the current measured in the presence of PKA within the corresponding section. Bars represent mean ± S.D. (n = 5-6). (C) WT CFTR data replotted from Fig. 4E and renormalised using the same procedure. For phosphorylated ΔF508 CFTR, the ratio of the current amplitude in the presence of PKA to that after PKA removal (B, centre and right panels; ratio of 2nd to 3rd bar), calculated individually for each patch, was 7.20 ± 4.33 (n = 6) in ATP and 13.3 ± 2.5 (n = 5) in P-ATP (mean ± S.D.). This ratio was significantly greater in P-ATP than in ATP (p = 0.0223, Student's 2-sample t-test). The ratio of the current amplitude in ATP after PKA removal to that in ATP + PKA (B-C, centre panels, third bar) was significantly smaller for ΔF508 than for WT ($p = 1.02 \times 10^{-5}$, Student's 2-sample t-test).*

4.1.3. The ΔF508 mutation slows both catalytic and noncatalytic activation by PKA

To determine whether the slowed activation of ΔF508 CFTR current (Fig. 5B, G) arises from delayed development of the catalytic or noncatalytic component, we quantified the contribution of each component to the total current at defined stages of the activation process. Patches were first exposed to 300 nM PKA for 1 minute and then for an

additional 3 minutes to ensure full phosphorylation (Fig. 7A). Following PKA washout, the remaining current indicates the magnitude of the irreversible (catalytic) component.

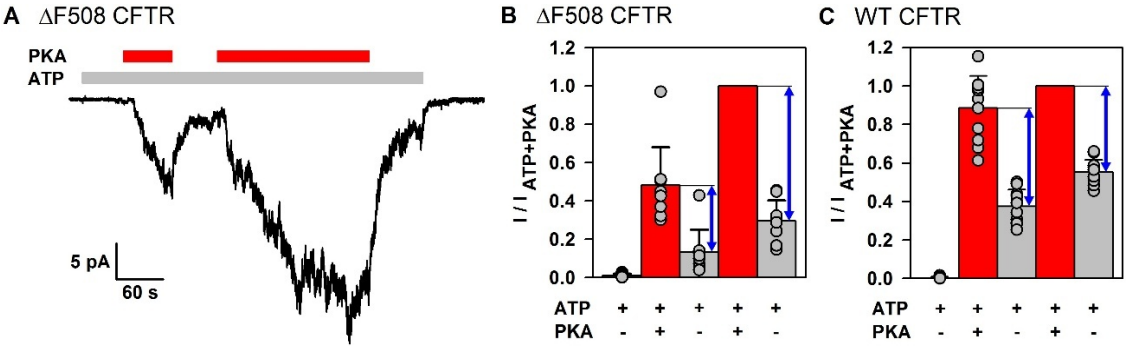

Figure 7. Both noncatalytic and catalytic activation by PKA develop more slowly for ΔF508 CFTR than for WT. *(A) Representative inside-out macroscopic patch recording of ΔF508 CFTR current elicited by consecutive 1-minute and 3-minute applications of 300 nM PKA (red bars) in the continuous presence of 2 mM ATP (light grey bar). (B-C) Mean currents measured over the final 20 s of each of the five consecutive segments of the protocol shown in (A) for ΔF508 (B) and WT (C) CFTR, normalised to the current during the second PKA exposure in the same patch. WT data in (C) are replotted from Mihályi et al. [13]. Bars represent mean ± S.D. (n = 7 for B; 11 for C). Blue double arrows indicate the magnitude of noncatalytic PKA stimulation after 1 minute of PKA exposure and after full phosphorylation, respectively. The ratio of noncatalytic stimulation after 1 minute versus 4 minutes in PKA+ATP (ratio of the first to the second blue arrow in B-C), calculated for each patch individually, was 0.51 ± 0.21 (n = 8) for ΔF508 and 1.16 ± 0.26 (n = 11) for WT CFTR (mean ± S.D.). This ratio was significantly smaller for ΔF508 than for WT ($p = 2.09 \times 10^{-5}$, Student's 2-sample t-test). The ratio of catalytic stimulation after 1 minute versus 4 minutes in PKA+ATP (ratio of the second to the third grey bar in B-C), calculated individually for each patch, was 0.44 ± 0.25 (n = 8) for ΔF508 and 0.68 ± 0.13 (n = 11) for WT CFTR (mean ± S.D.). This ratio was also significantly smaller for ΔF508 than for WT (p = 0.0128, Student's 2-sample t-test).*

Fig. 7B shows that for ΔF508 CFTR, after 1 min in ATP + 300 nM PKA, the reversible (noncatalytic) component has reached only ~50% of its maximal amplitude (Fig. 7B, blue double arrows), while the irreversible (catalytic) component has reached only ~45% of its maximum (Fig. 7B, grey bars). In comparison, for WT CFTR, the

reversible component was already fully developed (Fig. 7C, blue double arrows), and the irreversible component has reached ~70% of its maximal amplitude after 1 minute of PKA exposure under identical conditions (Fig. 7C, grey bars; from Mihályi et al. [13]). Therefore, the reduced overall activation rate of ΔF508 CFTR reflects a concomitant slowing in the development of both the reversible and the irreversible component.

4.1.4. Intact PKA binding for both ΔF508 and G551D CFTR

A previous study suggested a decreased PKA binding affinity for G551D [42]. To assess whether this could underlie the slowed activation kinetics observed for either of the mutants, phosphorylated ΔF508 and G551D channels gating in the presence of 2 mM ATP were sequentially exposed to 300 nM and 1.2 μM PKA (Fig. 8A-B). Within each patch, the amplitudes of reversible stimulation by the different PKA concentrations were directly compared (Fig. 8C-D). For both mutants, increasing the PKA concentration fourfold enhanced the reversible current component by only ~50% (Fig. 8C-D; compare blue double arrows), indicating that the apparent dissociation constant (K_d) for PKA binding is below 300 nM. This closely aligns with that previously determined for WT CFTR [12], indicating that the affinity for PKA binding is retained in both variants.

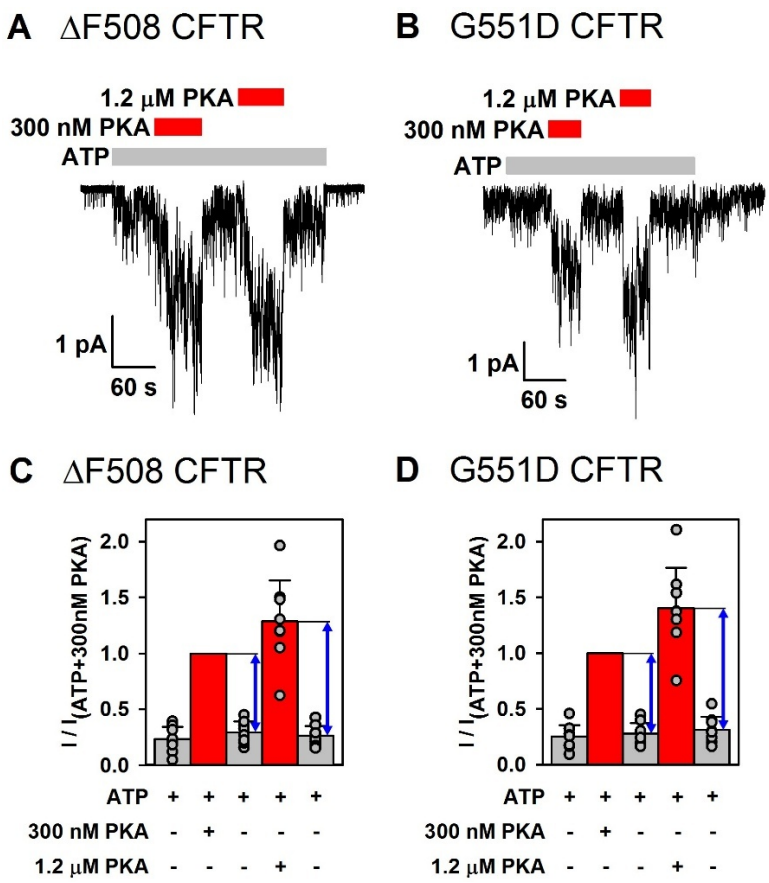

Figure 8. PKA binding affinity is preserved in ΔF508 and G551D CFTR. *(A-B) Quasi-macroscopic currents recorded from phosphorylated (A) ΔF508 and (B) G551D CFTR channels in the presence of 2 mM ATP (grey bars), illustrating noncatalytic stimulation by 300 nM or 1.2 μM PKA (red bars). (C-D) Mean steady-state currents measured during the five consecutive segments of the protocol shown in (A-B) for (C) ΔF508 and (D) G551D CFTR, normalised to the current recorded in 300 nM PKA within the same patch. Bars represent mean ± S.D. (n = 8 for both C and D). Blue double arrows indicate the magnitude of noncatalytic CFTR stimulation at 300 nM and 1.2 μM PKA.*

4.1.5. In the presence of potentiators, the reversible component of activation is undetectable for phosphorylated ΔF508, but is retained for G551D CFTR

Because most CF patients carrying ΔF508 alleles are currently treated with the ETI triple-combination therapy, we examined how the two potentiator components, elexacaftor and ivacaftor, together modulate PKA-dependent activation of ΔF508 CFTR. Unphosphorylated ΔF508 channels produced robust macroscopic currents in the

presence of 10 μM P-ATP, 1 μM elexacaftor and 10 nM ivacaftor, indicating notable drug-induced channel activation even prior to phosphorylation (Fig. 9A, left; cf. Fig. 4A, left). Exposing the channels to 300 nM PKA for 1 minute strongly enhanced these currents, demonstrating pronounced noncatalytic activation of unphosphorylated ΔF508 CFTR even in the presence of the potentiators (Fig. 9A-B).

Then, we examined PKA-dependent activation in the presence of ATP together with elexacaftor and ivacaftor (Fig. 9C-D). Once again, the exposure of unphosphorylated ΔF508 CFTR channels to ATP plus the drugs generated macroscopic currents, which increased by only ~2-3-fold during a 4-minute exposure to 300 nM PKA (Fig. 9C; Fig. 9D, 2nd vs 1st bar), in contrast to the ~80-fold stimulation observed in the absence of drugs (Fig. 4A, centre). Unexpectedly, removal of PKA in the continued presence of the drugs did not result in a significant current decrease, indicating a near-complete lack of noncatalytic stimulation of phosphorylated ΔF508 CFTR channels under these conditions (Fig. 9C, right; Fig. 9D, 3rd vs 2nd bar). Interestingly, noncatalytic stimulation of phosphorylated ΔF508 CFTR in the presence of ivacaftor alone has been demonstrated previously (Fig. 9E, replotted from Mihályi et al. [13]). In this study, we therefore also assessed PKA-dependent activation in the presence of elexacaftor alone (Fig. 9F-G). Under this condition, PKA dependence of ΔF508 CFTR activity closely resembled that reported for ivacaftor alone. Exposure of unphosphorylated ΔF508 channels to elexacaftor and ATP failed to elicit macroscopic currents (Fig. 9F, left; Fig. 9G, 1st bar). Following full channel activation, PKA removal triggered a rapid and pronounced current decline (Fig. 9F, right; Fig. 9G, 3rd vs 2nd bar). Taken together, these results demonstrate that noncatalytic stimulation of phosphorylated ΔF508 CFTR by PKA is preserved in the presence of either ivacaftor or elexacaftor alone but is abolished when both potentiators are applied simultaneously.

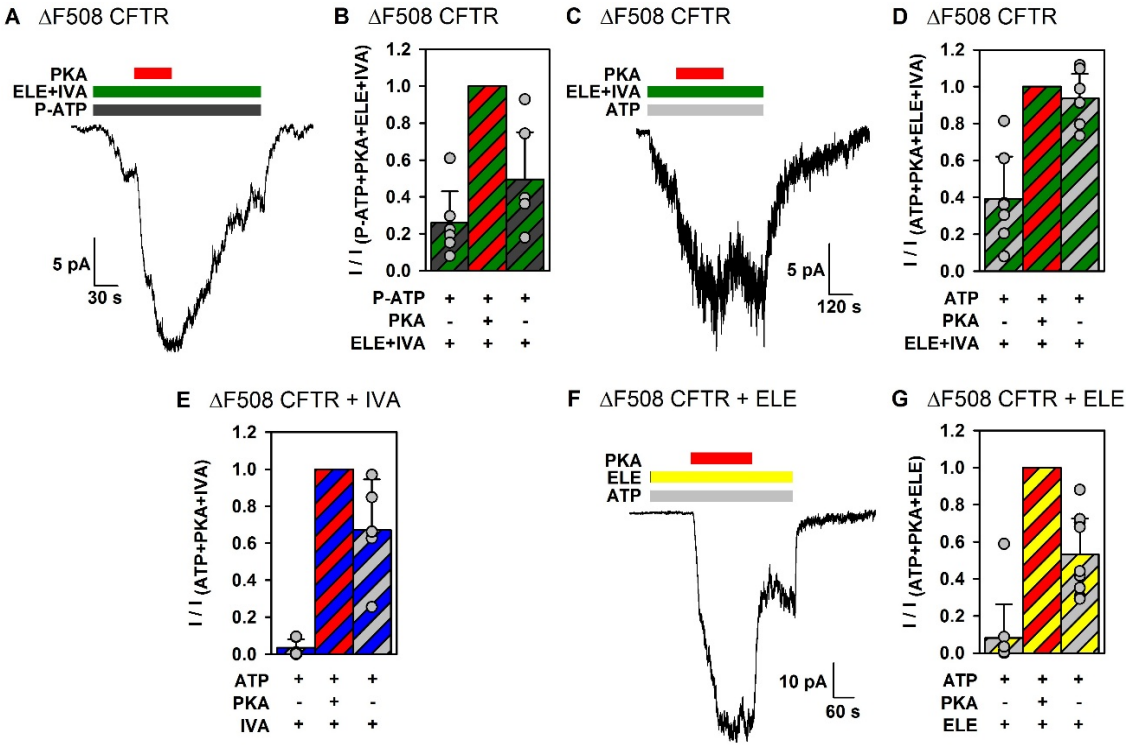

Figure 9. Effects of potentiator drugs ΔF508 CFTR. *(A) Representative macroscopic inside-out patch recording of unphosphorylated ΔF508 CFTR channels activated by 10 μM P-ATP (dark grey bar) in the presence of 1 μM elexacaftor + 10 nM ivacaftor (green bar), followed by application of 300 nM PKA (red bar). (B) Mean steady-state currents measured during the three consecutive segments of the protocol shown in (A), normalised to the mean current recorded during PKA exposure. Bars represent mean ± S.D. (n = 6). (C, F) Representative macroscopic inside-out patch recordings of ΔF508 CFTR channels in 2 mM ATP (light grey bars) in the presence of either 1 μM elexacaftor + 10 nM ivacaftor (C, green bar) or 1 μM elexacaftor alone (F, yellow bar). Steady-state currents were assessed before, during, and after full channel activation induced by a 3-4-minute superfusion with 300 nM PKA (red bars). (D, E, G) Fractional steady-state currents of ΔF508 CFTR channels in 2 mM ATP and the indicated drug condition, measured before PKA exposure (1st bars), in the presence of 300 nM PKA (2nd bars), and after PKA removal (3rd bars). Data in (E) are replotted from Mihályi et al. [13]. Bars represent mean ± S.D. (n = 7 for D; 5-6 for E; 9 for G). The ratio of the current amplitude after PKA removal to that in the presence of PKA (cf. B, D, E, G; 3rd bar) was significantly smaller than unity in (B) ($p = 2.37 \times 10^{-3}$), (E) ($p = 0.0271$), and (G) ($p = 4.32 \times 10^{-5}$), but not in (D) ($p = 0.125$) (one-tailed Student's 1-sample t-test).*

The absence of noncatalytic stimulation of ΔF508 CFTR by PKA in the presence of ATP + ivacaftor + elexacaftor was further confirmed in recordings from patches containing only a small number of active channels, enabling dwell-time analysis (Fig. 10A). The estimated open probability of phosphorylated channels in ATP + drugs remained ~0.5 and was unaffected by the presence or absence of PKA (Fig. 10A-B).

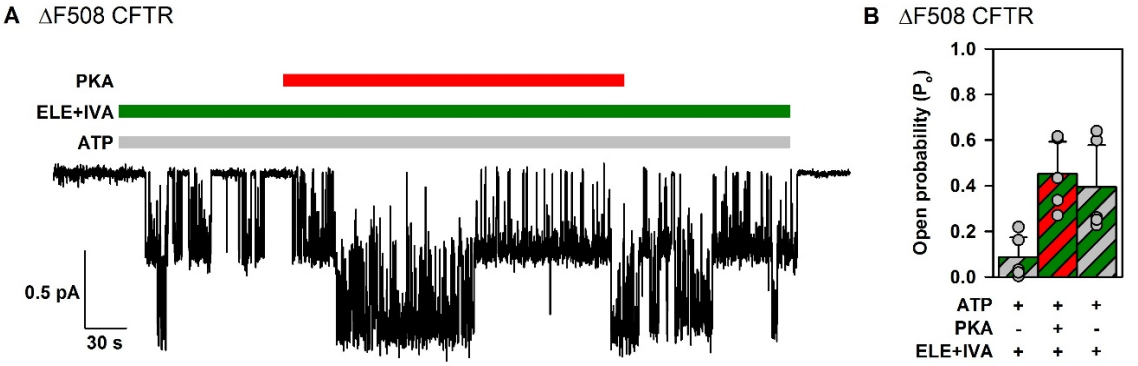

Figure 10. In the presence of ivacaftor + elexacaftor, the open probability of phosphorylated ΔF508 CFTR does not approach unity. *(A) Representative microscopic inside-out patch recording from two active ΔF508 CFTR channels in the presence of 2 mM ATP (light grey bar) and 1 μM elexacaftor + 10 nM ivacaftor (green bar). Steady-state gating was evaluated before, during, and after full channel activation induced by a 4-minute superfusion with 300 nM PKA (red bar). Recording temperature was 25°C. (B) Open probabilities (P_o) of ΔF508 CFTR channels in 2 mM ATP and 1 μM elexacaftor + 10 nM ivacaftor measured before PKA exposure (1st bar), in the presence of 300 nM PKA (2nd bar), and after PKA removal (3rd bar). Bars represent mean ± S.D. (n = 5). The P_o after PKA removal was not significantly smaller than that in the presence of PKA (p = 0.297, one-tailed Student's 2-sample t-test).*

Although most patients carrying a G551D allele can be treated with ivacaftor monotherapy, many, particularly those who also carry a ΔF508 allele, have transitioned to ETI therapy. In intact cells, combined treatment with elexacaftor and ivacaftor has been reported to increase forskolin-stimulated G551D CFTR activity by approximately two orders of magnitude [47]. We also examined how elexacaftor and ivacaftor modulate catalytic and noncatalytic PKA-dependent activation of G551D CFTR. PKA, applied to unphosphorylated channels gating in P-ATP in the presence of elexacaftor and ivacaftor, produced a pronounced reversible stimulation (Fig. 11A-B). Moreover,

currents from unphosphorylated G551D channels gating in ATP together with the two drugs were robustly enhanced by PKA, indicating that the open probability of unphosphorylated G551D CFTR remains low even in the presence of both potentiators (Fig. 11C, left; Fig. 11D, 1st vs 2nd bar). This behaviour contrasts with that observed for ΔF508 CFTR (Fig. 9C, left; Fig. 9D, 1st vs 2nd bar). Finally, removal of PKA revealed that about ~50% of the total current observed in the presence of ATP + PKA + drugs arose from reversible, noncatalytic stimulation (Fig. 11C, right; Fig. 11D, 2nd vs 3rd bar). Altogether, the elexacaftor-ivacaftor combination preserves and boosts both catalytic and noncatalytic components of activation of G551D CFTR channels.

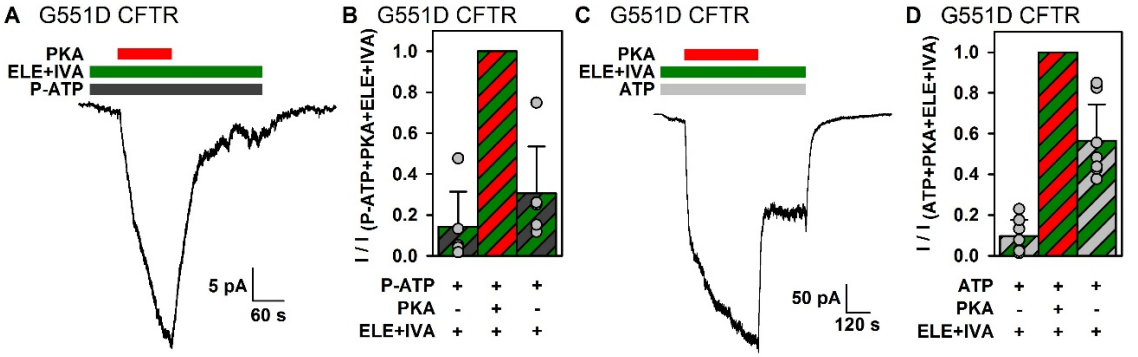

Fig. 11. Effects of potentiator drugs on noncatalytic and catalytic activation of G551D CFTR. *(A) Representative macroscopic inside-out patch recording of unphosphorylated G551D CFTR channels activated by 10 μM P-ATP (dark grey bar) in the presence of 1 μM elexacaftor + 10 nM ivacaftor (green bar), followed by application of 300 nM PKA (red bar). (B) Mean steady-state currents measured during the three consecutive segments of the protocol shown in (A), normalised to the mean current recorded during PKA exposure. Bars represent mean ± S.D. (n = 5). (C) Representative macroscopic inside-out patch recording of G551D CFTR channels in the presence of 2 mM ATP (light grey bar) and 1 μM elexacaftor + 10 nM ivacaftor (green bar). Steady-state currents were assessed before, during, and after full channel activation induced by a 4-minute superfusion with 300 nM PKA (red bar). (D) Mean steady-state currents measured during the three consecutive segments of the protocol shown in (C), normalised to the mean current recorded during PKA exposure. Bars represent mean ± S.D. (n = 7). The ratio of the current amplitude after PKA removal to that in the presence of PKA (B, D; third bar) was significantly smaller than unity in*

both (B) ($p = 1.21 \times 10^{-3}$) and (D) ($p = 3.36 \times 10^{-4}$) (one-tailed Student's 1-sample t-test).

4.2. Characterisation of rare, cystic fibrosis-causing mutations

4.2.1. Channel maturation of the five mutants is variously compromised and can be restored by the correctors

Normally, CFTR undergoes sequential glycosylation, beginning with core glycosylation in the ER and followed by complex glycosylation in the Golgi apparatus. As glycosylation decreases electrophoretic mobility, the different maturation states of CFTR can be separated by SDS-PAGE. Western blot analysis of wild-type (WT) CFTR typically reveals three distinct bands (Fig. 12A, left), corresponding to the non-glycosylated (Band A), core-glycosylated (Band B), and fully mature, complex-glycosylated (Band C) forms [71]. Class II CFTR mutations, including ΔF508, disrupt proper protein folding and maturation, resulting in ER retention and a marked reduction or absence of Band C [28].

To evaluate the impact of the five rare CFTR mutations on protein expression and maturation, we compared their electrophoretic migration profiles by western blot analysis of crude membrane preparations from HEK-293T cells transiently expressing each mutant construct (Fig. 12A). Densitometric quantification demonstrated a reduction in Band C intensity for all five variants relative to WT CFTR (Fig. 12C, light grey bars), with the most pronounced decreases observed for I336K and T465I, which reached approximately 38% and 14% of WT levels, respectively. In contrast, the intensities of Bands A and B were not reduced for any mutant. Consequently, the fractional contribution of Band C to total CFTR signal [C/(A + B + C)] was significantly diminished for I336K ($p = 0.0116$), T465I ($p = 4.99 \times 10^{-5}$), and T582I ($p = 0.0493$) (Fig. 12D, light grey bars). Given that Band C abundance correlates with CFTR surface expression [28, 72], these findings indicate reduced plasma membrane localisation of all mutant channels, with I336K and T465I exhibiting the most severe defects, classifying them as Class II mutants.

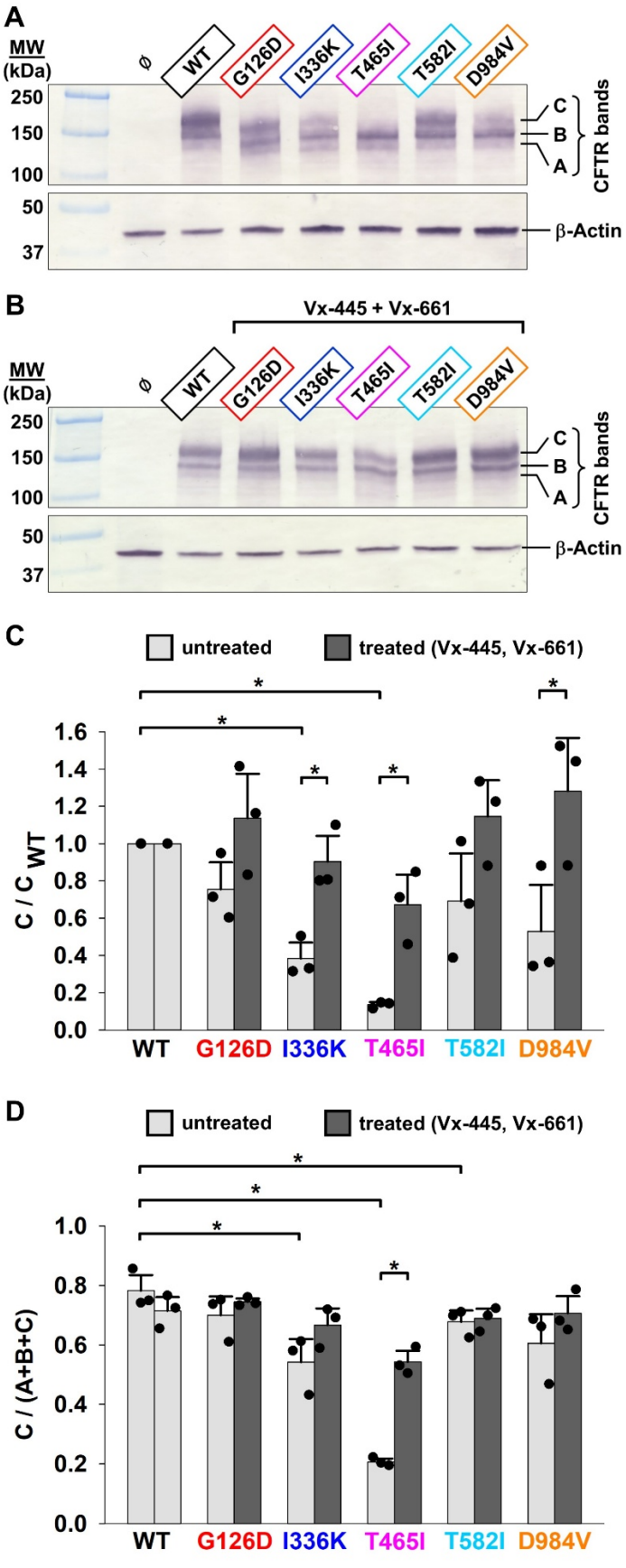
A
MW
(kDa)
250
150
100
50
37
ϕ
WT
G126D
I336K
T465I
T582I
D984V
C
B
A
CFTR bands
β-Actin
B
Vx-445 + Vx-661
C
untreated
treated (Vx-445, Vx-661)
C / C WT
1.6
1.4
1.2
1.0
0.8
0.6
0.4
0.2
0.0
WT
G126D
I336K
T465I
T582I
D984V
D
C / (A+B+C)

Figure 12. Impaired maturation of mutant CFTR channels and rescue by corrector treatment. *(A, B) Representative western blot analysis of wild-type (WT) and mutant CFTR constructs expressed in HEK-293T cells. Cells were either untreated (A) or incubated with 3 μM elexacaftor (VX-445) and 3 μM tezacaftor (VX-661) (B). In both panels, WT represents untreated WT-transfected cells, the negative control (lane Ø) indicates non-transfected cells, and β-actin (bottom panels) was used as a loading control. (C, D) Densitometric quantification of the blots shown in A (left column) and B (right column) for each construct. Band C densities of CFTR constructs without treatment (light grey bars; from A) and after corrector treatment (dark grey bars; from B) are shown normalised either to (C) untreated WT Band C levels on the same blot or to (D) the total CFTR signal (Bands A + B + C) of the respective construct. Data represent mean ± SD from three biologically independent experiments. Asterisks denote statistically significant differences ($P < 0.05$).*

The correctors tezacaftor and elexacaftor have been shown to effectively rescue the maturation of Class II CFTR mutants, including ΔF508 [73], as well as numerous rare variants [72]. To determine the responsiveness of the five CFTR mutants examined here, cells were treated for 24 hours with 3 μM tezacaftor and 3 μM elexacaftor before protein extraction [45, 72]; these drug concentrations are reportedly physiologically relevant [74, 75] and have been proven efficient for multiple CFTR variants *in vitro* [48, 76]. Corrector treatment increased Band C intensity for all five mutants (Fig. 12A vs Fig. 12B), and the magnitude of rescue inversely correlated with the baseline Band C levels observed under untreated conditions; the strongest responses were observed for T465I and I336K (Fig. 12C-D, dark versus light grey bars). All in all, the correctors restored Band C levels to near WT values for all mutants (Fig. 12C, dark grey bars).

4.2.2. While ATP affinity and activation by PKA remain intact, single-channel recordings reveal gating defects for G126D, T582I and D984V CFTR

WT CFTR and all five variants were expressed in *Xenopus laevis* oocytes and analysed using inside-out patch clamp recordings. Application of 2 mM ATP + 300 nM PKA activated large macroscopic currents for the G126D, T582I, and D984V mutants (Fig. 13B-D). In contrast, only sporadic pore openings were observed for I336K and T465I under identical conditions, even after injection of up to 30 ng of cRNA. Accordingly,

gating properties could be quantitatively characterised only for G126D, T582I, and D984V CFTR.

All three mutants (Fig. 13B-D) exhibited wild-type-like regulation by PKA, with negligible activity in ATP prior to PKA exposure, robust activation upon PKA application, and rapid partial deactivation following PKA washout. Notably, the fraction of current persisting after PKA removal (Fig. 13E, grey bars) was slightly but significantly reduced for all three mutants compared to WT ($p = 0.000597$, 0.00009, and 0.0223 for G126D, T582I, and D984V, respectively), suggesting a modest increase in the relative contribution of the reversible component to total channel activity in the mutants.

The ATP sensitivity of pre-phosphorylated channels was assessed by exposing patches containing multiple channels to various test ATP concentrations bracketed by applications of 3.2 mM ATP (Fig. 13F-I). All three mutants displayed intact ATP sensitivity, yielding dose-response curves indistinguishable from WT ($K_{1/2} \approx 50$ μM; Fig. 13J).

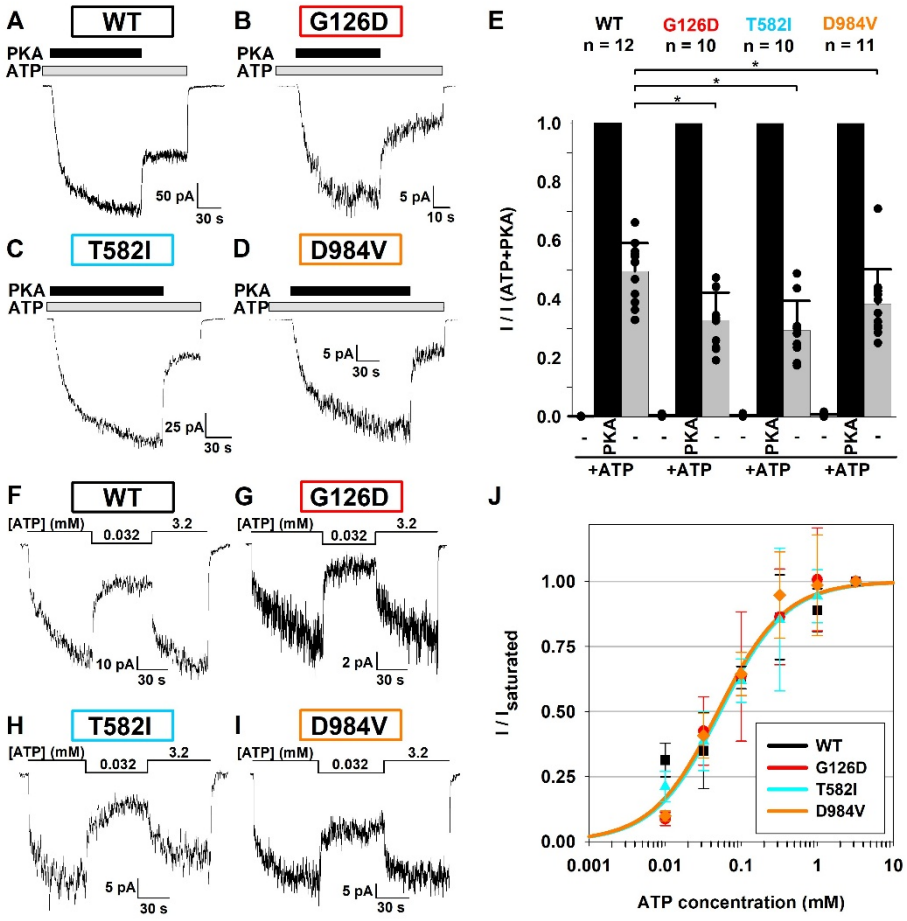

Figure 13. Mutant CFTR constructs retain normal PKA and ATP dependence of channel activity. *(A-D) Representative macroscopic inside-out patch currents recorded from WT (A), G126D (B), T582I (C), and D984V (D) CFTR channels during exposure to 300 nM PKA (black bars) in the presence of 2 mM ATP (grey bars). Membrane potential was −40 mV; downward deflections indicate channel openings. (E) Fractional channel activity before, during, and after PKA exposure. Steady-state currents measured prior to PKA application, during PKA exposure, and following PKA washout are shown normalised to currents in the presence of PKA (black bars). Bars represent mean ± SD, with the number of patches indicated; asterisks denote statistically significant differences ($p < 0.05$). (F-I) Representative macroscopic current traces from pre-phosphorylated WT (F), G126D (G), T582I (H), and D984V (I) CFTR channels during exposure to 32 μM ATP, bracketed by applications of 3.2 mM ATP. Membrane potential was −40 mV; downward deflections indicate channel openings. The displayed*

segments were recorded after 1-3 minutes of exposure to 2 mM ATP + 300 nM PKA, as shown in A-D. (J) ATP dose-response relationships for the channel constructs. Currents measured at various test ATP concentrations are normalised to the mean current during bracketing exposures to 3.2 mM ATP. Symbols represent mean ± SD (n = 5-14). Solid curves show fits to the Michaelis-Menten equation; $K_{1/2}$ values were 50 ± 10, 53 ± 7, 53 ± 4, and 50 ± 7 μM for WT, G126D, T582I, and D984V CFTR, respectively.

To compare steady-state gating kinetics of the mutant channels to the wild type, currents of pre-phosphorylated WT, G126D, T582I, and D984V CFTR were recorded in the presence of 2 mM ATP from patches containing only a few channels ($N \leq 5$), allowing individual gating events to be clearly resolved (Fig. 14A, left). To estimate channel number within each patch, 300 nM PKA was reapplied at the end of each recording to elicit noncatalytic stimulation, and ATP was replaced by 50 μM 2-deoxy-N^6-(2-phenylethyl)adenosine-5-O-triphosphate (P-dATP), a nucleotide analogue that directly stimulates CFTR gating by binding to its nucleotide-binding domains [30]. This protocol produces strong activation of CFTR channels [33] (Fig. 14A, right). Open probability (P_o), mean burst duration (T_b), and mean interburst duration (T_{ib}) were quantified by dwell-time analysis [67].

Compared to WT CFTR, P_o was only modestly reduced for D984V but was significantly decreased for G126D ($p = 0.00194$) and T582I ($p = 0.000195$) (Fig. 14B, right), classifying the latter two variants as Class III mutants. The kinetic mechanisms underlying the reduced P_o differed among mutants: for G126D, the P_o reduction resulted primarily from an increased closing rate, reflected by a shortened T_b ($p = 0.00266$), whereas for T582I it was caused by a decreased opening rate, manifested as a prolonged T_{ib} ($p = 0.000865$). In contrast, D984V exhibited an increased closing rate that was partially compensated by a concomitant increase in opening rate (Fig. 14B, bottom).

A

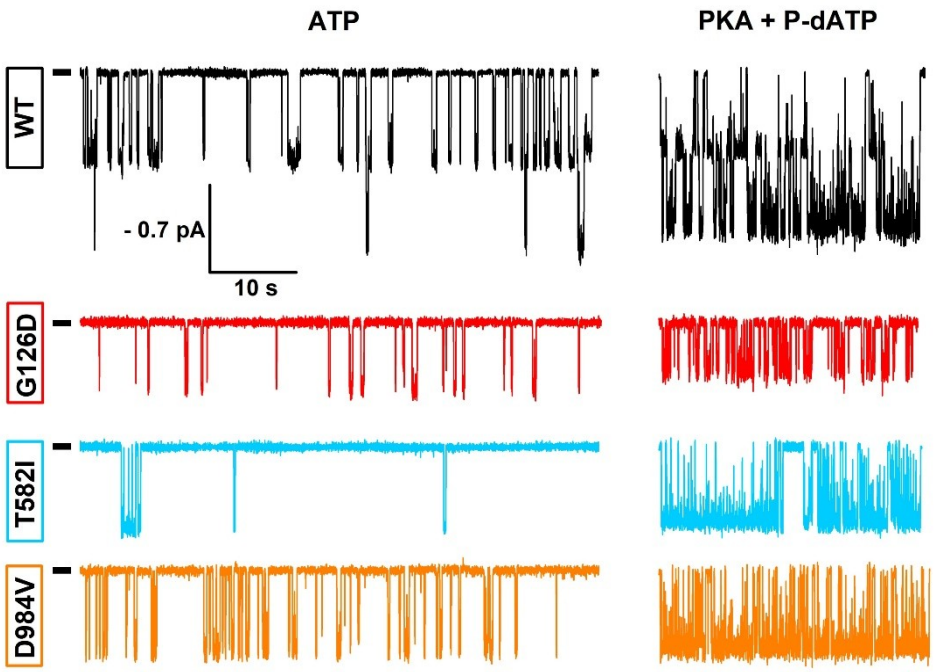

B

Construct	n	Parameter		
		Opening rate (s^{-1})	Closing rate (s^{-1})	P_o
WT	11	0.45 ± 0.24	2.56 ± 1.53	0.16 ± 0.06
G126D	11	0.46 ± 0.36	5.11 ± 1.93	0.08 ± 0.05
T582I	7	0.07 ± 0.03	1.41 ± 0.54	0.04 ± 0.03
D984V	10	0.62 ± 0.37	4.22 ± 1.24	0.12 ± 0.07

Figure 14. Single-channel recordings reveal reduced open probability of G126D and T582I CFTR. *(A) Representative single-channel current traces from two pre-phosphorylated WT channels and single pre-phosphorylated G126D, T582I, and D984V CFTR channels. Recordings were obtained in the presence of 2 mM ATP (left) and during subsequent exposure to 50 µM P-dATP plus 300 nM PKA (right). The membrane potential was held at -80 mV. Downward deflections indicate channel openings, and zero-current levels are marked by short black dashes. The displayed current segments were recorded after 1-3 minutes of exposure to 2 mM ATP and 300 nM PKA. (B) Kinetic parameters of channel gating derived from single-channel analysis. Opening rate ($1/T_{ib}$; s^{-1}), closing rate ($1/T_b$; s^{-1}), and open probability (P_o) are shown as mean ± SD; n denotes the number of patches analysed.*

4.2.3. Potentiators enhance gating of all five variants including I336K and T465I

We employed macroscopic inside-out patch-clamp recordings to determine the extent to which the gating defects of the G126D, T582I, and D984V CFTR variants can be rescued by potentiator drugs. In addition to the potentiator ivacaftor, the corrector elexacaftor has been shown to function as a co-potentiator that synergistically enhances CFTR gating [45-47]. Pre-phosphorylated channels gating in the presence of 2 mM ATP were first exposed to 10 nM ivacaftor (Fig. 15A-C), a clinically relevant free drug concentration [77] that is near-saturating for WT CFTR and many mutant channels [78, 79]. After current stabilisation, 1 μM elexacaftor was added (Fig. 15A-C), a concentration well above the reported EC_{50} values for co-potentiation (1-15 nM) across WT CFTR and multiple variants [45-47]. To achieve maximal stimulation, 300 nM PKA was subsequently reapplied, and ATP was replaced by 50 μM P-dATP, while maintaining both potentiators throughout (Fig. 15A-C). All three mutants responded robustly to the drugs combination (Fig. 15F; note logarithmic scale). Ivacaftor alone increased macroscopic currents by ~ 3-5-fold (Fig. 15F, 1st panel), while the addition of elexacaftor produced a further ~2-fold potentiation (Fig. 15F, 2nd panel). Consequently, the combined drug treatment enhanced currents by ~4-fold for D984V, ~6-fold for G126D, and ~10-fold for T582I. Despite this substantial rescue, the open probability (P_o) of all three mutants remained well below unity, as indicated by the additional current increases observed upon the application of PKA and subsequent substitution of ATP with P-dATP (Fig. 15F, 3rd and 4th panels).

Of note, the maximal stimulation achieved with the full stimulator cocktail provides an upper bound for the initial P_o in the presence of ATP alone. For T582I and D984V, these upper bounds are consistent with P_o values obtained from single-channel recordings (Fig. 14B). In contrast, for G126D the approximately 20-fold maximal stimulation (Fig. 15F, 4th panel, red symbol) implies an initial P_o of $\leq$~0.05, suggesting a slight overestimation of P_o in the single-channel analysis (Fig. 14), most likely due to uncertainties in determining channel number in the patch.

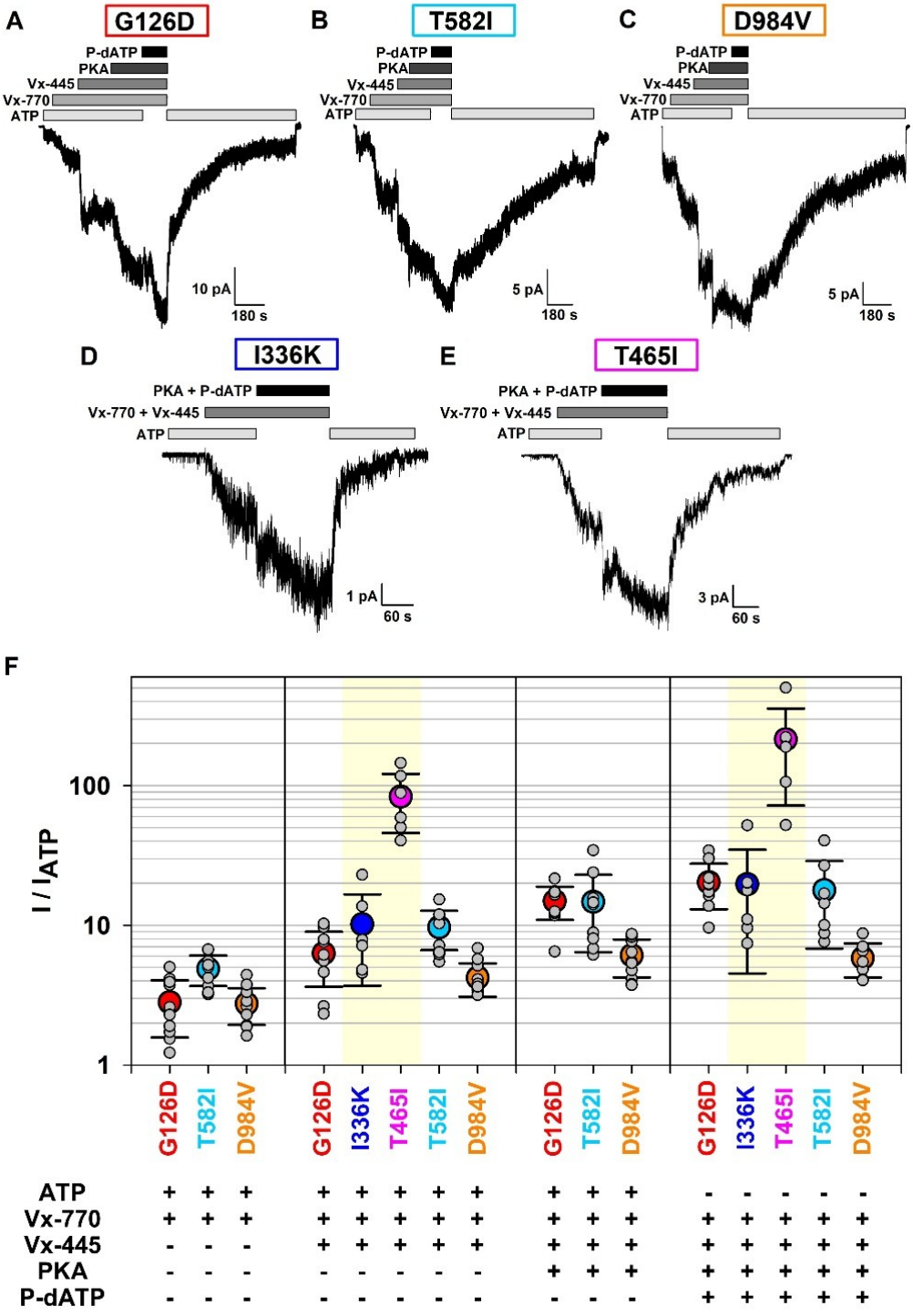

Figure 15. All mutant CFTR channels respond to potentiator treatment. *(A-E) Representative macroscopic currents recorded from pre-phosphorylated G126D (A), T582I (B), D984V (C), I336K (D), and T465I (E) CFTR channels in the presence of 2 mM ATP. Currents were measured during stepwise addition of CFTR stimulators: ivacaftor (VX-770) (10 nM), elexacaftor (VX-445) (1 μM), PKA (300 nM), and P-dATP*

(50 μM; replacing ATP). In panels D and E, VX-770 + VX-445 and PKA + P-dATP were applied pairwise. The membrane potential was held at -40 mV, and downward deflections represent channel openings. The displayed current segments were recorded after 1-3 minutes of exposure to 2 mM ATP and 300 nM PKA. (F) Fractional steady-state currents of mutant CFTR channels following incremental addition of the four potentiators, normalised to currents measured in the presence of ATP alone. Note the logarithmic y-axis. Symbols represent mean ± SD (n = 7-11). The faint yellow background in panels 2 and 4 indicates the modified experimental protocol (pairwise addition of stimulators) used for I336K and T465I.

For the I336K and T465I variants, the lack of macroscopic currents with PKA and ATP alone may only be partially attributed to their maturation defects (Fig. 12). We therefore tested whether these mutants also exhibit intrinsic gating defects and whether they respond to potentiator drugs. Indeed, exposure of pre-phosphorylated channels to 10 nM ivacaftor + 1 μM elexacaftor activated large macroscopic currents in both cases (Fig. 15D-E), corresponding to approximately 10-fold and 80-fold current increases for I336K and T465I, respectively (Fig. 15F, 2nd panel). Subsequent addition of PKA and P-dATP further enhanced these currents by roughly two-fold (Fig. 15D-E), yielding maximal fractional stimulations of ~20-fold for I336K and ~200-fold for T465I CFTR. These results imply that, in the presence of ATP alone, P_o is ≤~0.05 for phosphorylated I336K and ≤~0.005 for phosphorylated T465I, classifying both variants as Class III mutants as well.

Although even rough estimates of channel number in a patch are not feasible for the latter two mutants, dwell-time analysis of record segments obtained in ATP alone, prior to drug application (Fig. 15D-E, initial segments; cf. Fig. 16A), permits accurate estimation of the closing rate. Together with the upper bounds for P_o described above, this information allows calculation of an upper bound for the opening rate (see Methods). This detailed kinetic analysis again revealed distinct mechanisms underlying impaired gating in the two mutants. The closing rate was only modestly increased (T_b shortened) for T465I but markedly accelerated for I336K, whereas the opening rate was dramatically reduced (T_{ib} prolonged; >20-fold) for T465I but likely less affected for I336K (Fig. 16B).

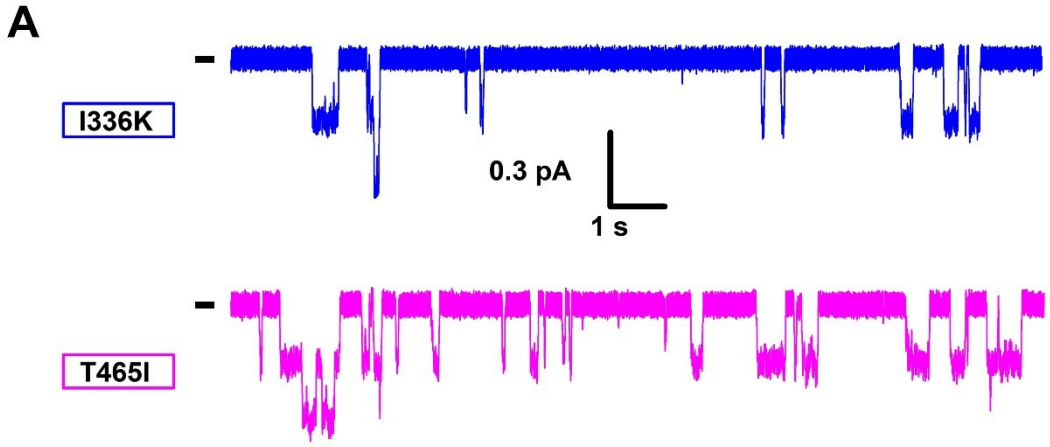

B

Construct	Parameter		
	Opening rate (s^{-1})	Closing rate (s^{-1})	P_o
WT	0.45 ± 0.24	2.56 ± 1.53	0.16 ± 0.07
I336K	≤ 0.2699	5.86 ± 3.63	≤ 0.0440
T465I	≤ 0.0161	3.10 ± 1.41	≤ 0.0052

Figure 16. Single-channel gating parameters of I336K and T465I CFTR mutants. *(A) Representative resolvable unitary openings of pre-phosphorylated I336K and T465I CFTR channels gating in 2 mM ATP, recorded from patches containing hundreds of channels prior to the addition of potentiator drugs (cf. Fig. 15D-E). Membrane potential was −40 mV; downward deflections indicate channel openings. The displayed segments were recorded after 1-3 minutes of exposure to 2 mM ATP + 300 nM PKA (cf. Fig. 13A-D). (B) Kinetic gating parameters in 2 mM ATP for I336K and T465I CFTR, including opening rate ($1/T_{ib}$; s^{-1}), closing rate ($1/T_b$; s^{-1}), and open probability (P_o). Closing rates were estimated directly and are shown as mean ± SD (n = 8 and 9 for I336K and T465I, respectively). An upper bound for P_o was derived from the maximal fractional stimulation by drugs (cf. Fig. 15F, fourth panel), and the corresponding upper bound for opening rate was calculated as described in Methods. WT gating parameters are replotted from Fig. 14B.*

4.2.4. Small reductions in unitary current amplitude for G126D, I336K, and T465I

Single-channel current amplitudes for T582I and D984V CFTR were similar to that of WT (Fig. 14A), whereas visibly smaller amplitudes were observed for the remaining three mutants. To quantify these differences, unitary conductances were determined by

measuring single-channel current amplitudes at membrane potentials of -80, -40, and +40 mV (Fig. 17A-D). Linear regression of the resulting current-voltage relationships yielded slope conductances for each variant (Fig. 17E). Relative to WT CFTR (7.3 ± 0.6 pS), unitary conductance was modestly but significantly reduced for G126D (6.1 ± 0.1 pS; p = 0.00270), I336K (5.0 ± 0.3 pS; p = 0.00001), and T465I (6.4 ± 0.5 pS; p = 0.00975), classifying these three variants also as Class IV mutants.

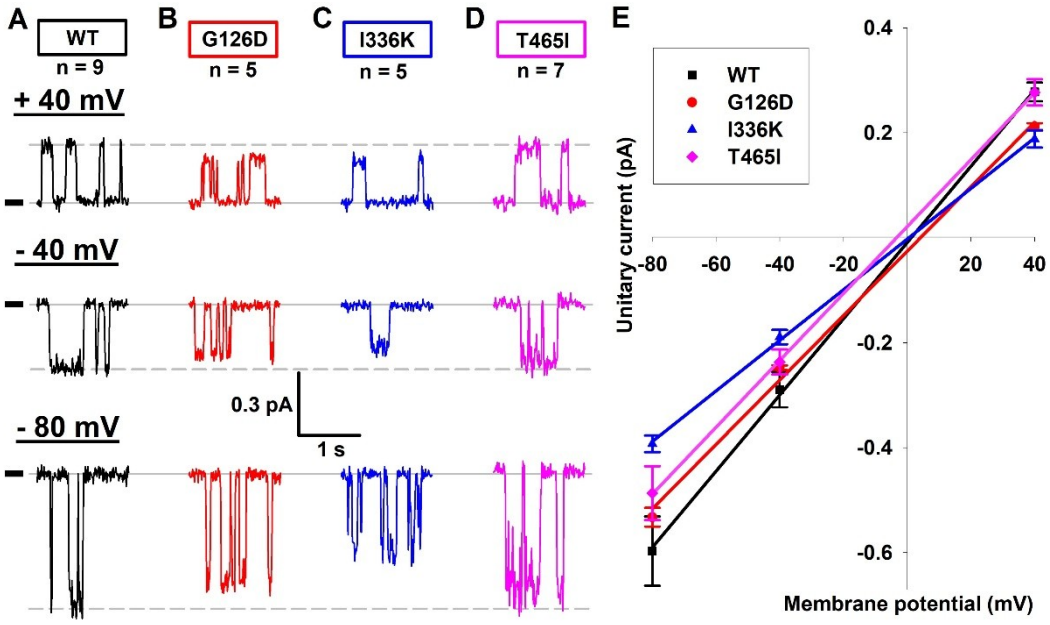

Figure 17. Reduced unitary conductance of G126D, I336K, and T465I CFTR channels. (A-D) Representative single-channel openings recorded at membrane potentials of +40, -40, and -80 mV for WT (A), G126D (B), I336K (C), and T465I (D) CFTR channels; *n* indicates the number of patches analysed. Short black dashes and continuous grey lines denote zero-current levels, while dashed grey lines mark the open-channel current levels of WT CFTR. (E) Unitary current-voltage relationships (symbols) with corresponding linear fits (lines), yielding slope conductances of 7.3 ± 0.6 pS (WT), 6.1 ± 0.1 pS (G126D), 5.0 ± 0.3 pS (I336K), and 6.4 ± 0.5 pS (T465I). Symbols represent mean ± SD.

5. Discussion

5.1. Interactions of the ΔF508 and G551D mutations and the catalytic subunit of PKA

Both phosphorylated ΔF508 and G551D CFTR exhibit open probabilities in the presence of ATP and PKA orders of magnitude lower than WT CFTR [30, 31, 36]. Given that for WT CFTR, the catalytic and noncatalytic components of PKA-induced channel activity each contribute approximately half of the total activity [13], the pronounced reduction in P_o of the mutants implies that both components must be compromised. In the present study, we therefore examined how these two components are affected by the ΔF508 and G551D mutations.

Both catalytic and noncatalytic components of PKA-induced activity were detectable for both mutants (Fig. 4) and appeared to operate through mechanisms broadly similar to those of WT CFTR (Fig. 5). However, in both cases, overall activity was dominated by the reversible, noncatalytic component, which accounted for approximately 75% of the total current measured in the presence of ATP and PKA (Fig. 5C, F, G, H). Thus, both mutations impair catalytic activation proportionately more. In terms of the simplified kinetic scheme (Fig. 1), this corresponds to a disproportionate reduction in the P_o of compound states 2 and 5 relative to that of compound states 3 and 4.

Consistent with earlier reports [39, 41], the time course of current activation upon exposure to PKA and ATP was modestly slowed for G551D CFTR (Fig. 5E) and substantially slowed for ΔF508 CFTR (Fig. 5B). For ΔF508 CFTR, this delay reflected slower development of both the reversible and irreversible component (Fig. 7). In the kinetic scheme (Fig. 1), such behaviour could be attributed to a reduced equilibrium constant for PKA binding (steps 2→3 and 5→4), as previously suggested for G551D CFTR [42]. However, apparent affinities for PKA binding – estimated from the amplitudes of reversible current activation – were not reduced for either mutant relative to WT CFTR (Fig. 8; cf. Fiedorczuk et al. [12]). This implies that steps 2→3 and 5→4 likely represent compound processes involving both kinase binding at the NBD1-TMD interface and a subsequent conformational change which results in channel activation.

This study suggests that it is the latter step that is slowed by both mutations, not PKA binding.

Previous studies reported that P-ATP enhances the catalytic component of channel activity (the P_o of phosphorylated channels gating in the absence of PKA) for both ΔF508 and G551D CFTR [30, 80]. In the present study, this effect was reproduced for G551D CFTR (Fig. 4B; Fig. 4D, right, light vs dark grey bars), but not for ΔF508 CFTR (Fig. 4A; Fig. 4C, right, light vs grey bars). The basis for this discrepancy is uncertain but may reflect differences in experimental protocols. In particular, the 1-minute ATP removal used here may have induced partial channel inactivation [81]. Alternatively, the $K_{1/2}$ for gating stimulation under our conditions may be slightly higher than previously reported (~6 μM by Bompadre et al. [80]), such that 10 μM P-ATP remained subsaturating. Nevertheless, we observed a marked enhancement of noncatalytic PKA-dependent stimulation when channel gating was driven by P-ATP rather than ATP (Fig. 4) for both mutants, approximately 2-fold for ΔF508 CFTR and nearly 10-fold for G551D CFTR. This indicates that P-ATP can not only mitigate gating defects but also boost channel activation by PKA.

From a structural standpoint, it is noteworthy that the ΔF508 and G551D mutations, which perturb ATP-dependent gating through distinct mechanisms, produce strikingly similar defects in PKA-dependent activation. While ΔF508 primarily disrupts the NBD1-TMD interface, G551D targets the NBD1-NBD2 interface (Fig. 1B). Despite the differences in location, both mutations destabilise the NBD dimer interface [31, 32, 37, 82], an effect that can be partially stabilised by P-ATP [31, 82]. In addition, structural studies reveal that both mutations also impair the NBD1-TMD interface [27, 82].

Surprisingly, P-ATP not only stabilises the NBD1-NBD2 interface for both mutants, but at least for G551D also the NBD1-TMD interface [82]. Structure-function studies on the CFTR-PKA interaction [12, 13] suggest that docking of an R-domain loop at the NBD1-TMD interface is required for noncatalytic activation. Based on these facts, we speculate that these mutations could disrupt noncatalytic stimulation by destabilising the NBD1-TMD interface, which forms the docking site of the R-domain loop, whereas P-ATP might enhance noncatalytic stimulation by PKA for the mutants by stabilising that interface.

The obtained apparent affinities of both mutants for PKA (Fig. 8) contrast with earlier reports of a pronounced rightward shift in the PKA dose-response curve for G551D CFTR [42]. This discrepancy highlights the need to reconsider the interpretation of PKA dose-response relationships. Early studies proposed that endogenous phosphatases remain associated with excised patches [83, 84], leading to the view that PKA dose-response curves reflect the functional readout of progressively increasing steady-state phosphorylation stoichiometries of the R domain [42, 85]. This interpretation was revised following the demonstration that the rapid partial current decay upon PKA removal reflects loss of reversible stimulation by bound PKA rather than dephosphorylation. Indeed, phosphatases are unlikely to be present in excised patches, as full phosphorylation can be achieved even at low PKA concentrations, given sufficient exposure time [16]. Reversible stimulation, on the other hand, requires higher free PKA concentrations. Because the irreversible current component of G551D CFTR is very small (Fig. 5F), notable currents are observed only at higher PKA concentrations sufficient to elicit reversible activation. Moreover, in the study by Wang et al. [42], stimulation at high PKA concentrations may have been influenced by inorganic phosphate (P_i) present in the enzyme preparation, which strongly stimulates WT CFTR [16].

Finally, in the context of widespread ETI therapy, it is important to consider how elexacaftor and ivacaftor affect catalytic versus noncatalytic PKA-dependent activation. We show that, for both ΔF508 and G551D CFTR, the drug combination preferentially enhances the catalytic component, thereby reducing the relative contribution of noncatalytic activation to total current (Fig. 9C-D vs Fig. 5C, G, and Fig. 11C-D vs Fig. 5F, H). For phosphorylated ΔF508 CFTR in the presence of both drugs, noncatalytic stimulation is barely detectable (Fig. 9C-D). This cannot be readily explained by saturation of P_o, reaching unity, as single-channel analysis indicates a P_o of only ~0.5 under these conditions (Fig. 10). Interference with PKA docking also seems unlikely, as noncatalytic stimulation is preserved in the presence of either ivacaftor or elexacaftor alone (Fig 9E-G) and the drug binding sites do not overlap with that of PKA (Fig. 1A).

Regardless of the mechanism, these results point to opportunities for further modulator development. Drug combinations that enhance both irreversible and reversible PKA-dependent activation – analogous to the effects observed with P-ATP – may yield

additional functional benefit. Moreover, strategies that preserve strict PKA dependence of ΔF508 CFTR activity could represent an advance over current therapies, which elicit substantial PKA-independent channel activity (Fig. 9D, 1st bar).

5.2. Characteristics of rare cystic fibrosis-causing variants

We aimed to characterise five rare CFTR mutations identified in Hungarian CF patients, four of which have also been reported in other populations. For three of these variants – T582I, I336K, and G126D – maturation defects had also been described recently [57, 72, 86]. I336K was reported to respond to the corrector-potentiator combination ivacaftor + lumacaftor [86], and both I336K and G126D were identified as responsive to ETI treatment in a recent screening study [72]. However, detailed functional analyses were lacking for all five variants, and T465I and D984V had never been investigated previously.

Here, we show that all five variants display complex phenotypes that place each mutation into multiple mechanistic classes. All five exhibited impaired maturation, as indicated by defective glycosylation, with the most pronounced defect observed for T465I (Fig. 12A, Band C). For T582I, I336K, and G126D, the reductions in mature Band C densities were somewhat less severe than those reported previously [57, 72, 86]. This discrepancy likely reflects differences in experimental cell lines – HEK293-T cells in the present study versus HeLa, Fischer rat thyroid, or CFBE cells in the earlier works – as well as the inherently semi-quantitative nature of densitometric analysis. Nonetheless, all studies are consistent in assigning these three variants to Class II. Importantly, for all five mutations, glycosylation could be restored to near-WT levels by treatment with the corrector combination tezacaftor + elexacaftor (Fig. 12C, dark grey bars). Of note, because crude membrane preparations were used, our western blot analysis confirms only improved maturation but does not directly demonstrate increased plasma membrane expression.

PKA-dependent activation could be investigated for G126D, T582I and D984V, for which both catalytic and noncatalytic components of channel activation were readily detectable (Fig. 13A-D). Interestingly, the fractional contribution of the irreversible component was significantly smaller for the mutants than for WT (Fig. 13E, grey bars),

suggesting that the mutations reduce irreversible stimulation (via phosphorylation) to a greater extent than reversible stimulation mediated by PKA binding. None of the mutations altered the apparent ATP affinity ($K_{1/2}$) (cf. Fig. 13F-J). Of note, for I336K and T465I, 2 mM ATP was also saturating, with $I_{10\ mM\ ATP}/I_{2\ mM\ ATP}$ ratios of 0.96 ± 0.09 (n = 3) and 0.90 ± 0.13 (n = 2), respectively. Because $K_{1/2}$ reflects the ATP affinity of Site 2 in the closed channel [87, 88], these results indicate that ATP binding at Site 2 is not impaired by the mutations.

All five mutations reduced the steady-state open probability (P_o) of phosphorylated channels, with T465I producing the most severe decrease. However, the underlying kinetic mechanisms differed among variants. For G126D and I336K, the reduction in P_o was driven primarily by an increased closing rate (Figs. 14B, 16B), whereas for T582I it resulted mainly from a reduced opening rate (Fig. 14B). T465I affected both opening and closing rates (Fig. 16B). This pattern is consistent with previous observations that perturbations at the Site-2 NBD interface preferentially affect opening rates, mutations at the Site-1 NBD interface influence both opening and closing rates, and perturbations near the extracellular ends of the transmembrane domains primarily accelerate closing rates [33, 89]. In contrast, for the D984V mutant, an accelerated closing rate was partially compensated by an increased opening rate (Fig. 14B), suggesting a more complex effect of the mutation on gating energetics.

The multiplicative effects of ivacaftor, elexacaftor, PKA, and P-dATP on macroscopic currents (Fig. 15) support the existence of distinct binding sites for the two modulators [27], for PKA [12], and for the nucleotide analogue [12]. Importantly, for all five variants, currents were robustly enhanced by the potentiators, and noncatalytic stimulation by PKA remained clearly detectable even in the presence of the drugs.

Three mutations – G126D, I336K, and T465I – also caused modest reductions in unitary conductance (Fig. 17). While this finding is readily explained for G126D and I336K, which affect residues near the pore (Fig. 3), it was surprising for T465I, which targets NBD1, far from the selectivity filter.

Although reductions in channel number N, P_o, or unitary current amplitude (i) were observed for all five variants, the severity of these effects varied widely (Fig. 18). By categorising the reductions of these parameters as mild (60-90% of WT), substantial

(30-60% of WT), or severe (0-30% of WT), we estimate the following rank order of mutation-induced impairment of whole-cell CFTR current ($I_{CFTR}=N \cdot P_o \cdot i$): T465I > I336K > T582I > G126D > D984V. These estimates are subject to important limitations. First, the biophysical parameters were measured in heterologous expression systems, whereas CFTR expression and function in patients may be influenced by genetic background and environmental factors [90]. Second, these rare variants are rarely encountered in the homozygous state; therefore, clinical severity will also depend on the mutation present on the second allele. The predicted rank order is thus most relevant for cases in which the variant occurs in trans with a null allele, although clinical data for such genotypes are limited. Notably, I336K in trans with ΔF508 has been associated with both mild (pancreatic sufficient) and severe (pancreatic insufficient) disease phenotypes [55].

Mutation	Pathomechanism			Response to modulators	
	Class II (expression)	Class III (gating)	Class IV (permeation)	Correctors (Vx-445, Vx-661)	Potentiators (Vx-445, Vx-770)
G126D	↓	↓↓*	↓	✓	✓✓
I336K	↓↓	↓↓↓	↓	✓✓	✓✓
T465I	↓↓↓	↓↓↓	↓	✓✓	✓✓✓
T582I	↓	↓↓↓	→	✓	✓✓
D984V	↓↓	↓	→	✓✓	✓

Figure 18. Classification of the mutants by pathomechanism and their response to modulators. *Left: Summary of the effects of the five mutations on channel expression/maturation (quantified by Band C density), gating (quantified by P_o), and permeation (quantified by unitary conductance). Each parameter was classified as mildly (60-90% of WT; ↓), substantially (30-60% of WT; ↓↓), or severely (0-30% of WT; ↓↓↓) impaired. Right: Summary of the responses of the five mutants to modulators. Enhancement of expression/maturation by correctors was categorised as not significant (√) or significant (√√). Gating stimulation by potentiators was classified as modest (<5-fold; √), strong (5-20-fold; √√), or excessive (>20-fold; √√√).*
∗ For G126D, the P_o value of 0.08 (Fig. 14B) is likely overestimated, given its ~20-fold stimulation by drugs (Fig. 15F, 4th panel).

Crucially, all five variants were responsive to clinically approved CFTR modulators. The corrector combination tezacaftor + elexacaftor improved glycosylation for all mutants, with significant effects for T465I, I336K, and D984V, which exhibited the most severe maturation defects. In addition, the potentiator combination ivacaftor + elexacaftor significantly enhanced currents for all five variants. This stimulation can be assigned as modest for D984V, strong for G126D, I336K, and T582I, and exceptionally large for T465I. Together, these findings predict that ETI treatment should result in substantial restoration of CFTR-mediated anion transport in patients carrying any of these five mutations.

In summary, our data support the recent classification of G126D and I336K as ETI-eligible variants. Moreover, the functional evidence presented here strongly suggests that patients carrying T465I, T582I, or D984V alleles are also likely to benefit from ETI therapy.

6. Conclusions

6.1. Interactions of the ΔF508 and G551D mutants and the catalytic subunit of PKA

- For ΔF508 and G551D CFTR, non-catalytic activation dominates overall channel activity and may be further enhanced by stabilisation of the NBD1-NBD2-TMD interface via P-ATP.
- Both ΔF508 and G551D mutants exhibit slowed PKA-dependent activation, despite retaining normal binding affinity for the kinase.
- For ΔF508 CFTR, clinically used potentiators induce substantial PKA-independent activity, but also suppress non-catalytic activation of phosphorylated channels.

6.2. Characterisation of rare, cystic fibrosis-causing mutations

- Channel glycosylation is mildly impaired for G126D and T582I, substantially reduced for I336K and D984V, and severely disrupted for T465I. Treatment with clinically approved corrector compounds restores glycosylation to near wild-type levels.
- Channel open probability is mildly reduced for D984V, substantially decreased for G126D, and severely impaired for I336K, T465I, and T582I. Potentiator treatment markedly improves channel gating, resulting in substantial increases in macroscopic currents across all five variants.
- Channel conductance is mildly decreased for mutations G126D, I336K, and T465I.
- Collectively, these *in vitro* findings suggest that ETI therapy is likely to provide clinical benefit for patients carrying any of these five mutations.

7. Summary

This thesis examines the mechanisms by which CFTR maturation, PKA-dependent channel activation, gating, and permeation are impaired by common and rare CFTR mutations, as well as pharmacological rescue of these phenotypes. By integrating biochemical, kinetic, and pharmacological analyses, the work links molecular defects to mutation-specific responses to clinically approved modulators.

In the first study, we dissected catalytic and noncatalytic components of PKA-induced CFTR activation for WT channels and for the common disease-causing mutants ΔF508 and G551D. Although both mutants exhibit severely reduced open probability, both components of PKA-dependent activation remain present. However, catalytic activation is disproportionately impaired, resulting in channel activity being dominated by the noncatalytic component. Slowed activation kinetics were not caused by reduced PKA binding affinity but instead reflect impaired post-binding conformational transitions. Structural considerations implicate destabilisation of the NBD dimer and the NBD1-TMD interfaces as a shared mechanism. Stabilisation of these interfaces by the ATP analogue P-ATP alleviated both gating and activation defects, whereas the clinically used modulators elexacaftor and ivacaftor preferentially enhanced catalytic activation, reducing the relative contribution of reversible PKA-dependent stimulation.

In the second study, we characterised five rare CFTR mutations (T465I, T582I, I336K, G126D, and D984V) identified in Hungarian CF patients. All variants formed functional channels but displayed complex, multi-class defects involving impaired maturation, altered gating, and reduced conductance. Maturation defects were corrected by the corrector combination tezacaftor + elexacaftor, and all variants responded robustly to potentiation by ivacaftor + elexacaftor. PKA-dependent activation was preserved for all mutants, although catalytic activation was selectively reduced, consistent with findings from the first study. None of the mutations impaired ATP binding at Site 2, but each altered gating kinetics in a manner consistent with its structural location. By linking molecular mechanisms to mutation-specific drug responses, this work supports expanded eligibility for ETI therapy and contributes to the development of more precise, mechanism-based treatments for cystic fibrosis.

8. References

1. Bell, S.C., et al., *The future of cystic fibrosis care: a global perspective.* Lancet Respir Med, 2020. **8**(1): p. 65-124.
2. De Boeck, K. and M.D. Amaral, *Progress in therapies for cystic fibrosis.* Lancet Respir Med, 2016. **4**(8): p. 662-674.
3. O'Sullivan, B.P. and S.D. Freedman, *Cystic fibrosis.* Lancet, 2009. **373**(9678): p. 1891-904.
4. Mall, M.A., et al., *Cystic fibrosis.* Nat Rev Dis Primers, 2024. **10**(1): p. 53.
5. Quinton, P.M., *Cystic fibrosis: a disease in electrolyte transport.* FASEB J, 1990. **4**(10): p. 2709-17.
6. Barry, P.J., et al., *Triple Therapy for Cystic Fibrosis Phe508del-Gating and -Residual Function Genotypes.* N Engl J Med, 2021. **385**(9): p. 815-825.
7. Farrell, P.M., et al., *Guidelines for diagnosis of cystic fibrosis in newborns through older adults: Cystic Fibrosis Foundation consensus report.* J Pediatr, 2008. **153**(2): p. S4-S14.
8. Anderson, M.P., et al., *Demonstration that CFTR is a chloride channel by alteration of its anion selectivity.* Science, 1991. **253**(5016): p. 202-5.
9. Bear, C.E., et al., *Purification and functional reconstitution of the cystic fibrosis transmembrane conductance regulator (CFTR).* Cell, 1992. **68**(4): p. 809-18.
10. Riordan, J.R., et al., *Identification of the cystic fibrosis gene: cloning and characterization of complementary DNA.* Science, 1989. **245**(4922): p. 1066-73.
11. Taylor, S.S., et al., *Assembly of allosteric macromolecular switches: lessons from PKA.* Nat Rev Mol Cell Biol, 2012. **13**(10): p. 646-58.
12. Fiedorczuk, K., et al., *The structures of protein kinase A in complex with CFTR: Mechanisms of phosphorylation and noncatalytic activation.* Proc Natl Acad Sci U S A, 2024. **121**(46): p. e2409049121.
13. Mihalyi, C., et al., *Structural determinants of protein kinase A essential for CFTR channel activation.* Proc Natl Acad Sci U S A, 2024. **121**(46): p. e2407728121.

14. Liu, F., et al., *Molecular Structure of the Human CFTR Ion Channel.* Cell, 2017. **169**(1): p. 85-95 e8.
15. Zhang, Z., F. Liu, and J. Chen, *Molecular structure of the ATP-bound, phosphorylated human CFTR.* Proc Natl Acad Sci U S A, 2018. **115**(50): p. 12757-12762.
16. Mihalyi, C., et al., *Simple binding of protein kinase A prior to phosphorylation allows CFTR anion channels to be opened by nucleotides.* Proc Natl Acad Sci U S A, 2020. **117**(35): p. 21740-21746.
17. Aleksandrov, L., et al., *The First Nucleotide Binding Domain of Cystic Fibrosis Transmembrane Conductance Regulator Is a Site of Stable Nucleotide Interaction, whereas the Second Is a Site of Rapid Turnover.* J Biol Chem, 2002. **277**(18): p. 15419-25.
18. Basso, C., et al., *Prolonged nonhydrolytic interaction of nucleotide with CFTR's NH2-terminal nucleotide binding domain and its role in channel gating.* J Gen Physiol, 2003. **122**(3): p. 333-48.
19. Vergani, P., et al., *CFTR channel opening by ATP-driven tight dimerization of its nucleotide-binding domains.* Nature, 2005. **433**(7028): p. 876-80.
20. Levring, J., et al., *Author Correction: CFTR function, pathology and pharmacology at single-molecule resolution.* Nature, 2023. **617**(7961): p. E11.
21. Szollosi, A., et al., *Mutant cycles at CFTR's non-canonical ATP-binding site support little interface separation during gating.* J Gen Physiol, 2011. **137**(6): p. 549-62.
22. Tsai, M.F., M. Li, and T.C. Hwang, *Stable ATP binding mediated by a partial NBD dimer of the CFTR chloride channel.* J Gen Physiol, 2010. **135**(5): p. 399-414.
23. Haardt, M., et al., *C-terminal truncations destabilize the cystic fibrosis transmembrane conductance regulator without impairing its biogenesis. A novel class of mutation.* J Biol Chem, 1999. **274**(31): p. 21873-7.
24. Welsh, M.J. and A.E. Smith, *Molecular mechanisms of CFTR chloride channel dysfunction in cystic fibrosis.* Cell, 1993. **73**(7): p. 1251-4.
25. Zielenski, J. and L.C. Tsui, *Cystic fibrosis: genotypic and phenotypic variations.* Annu Rev Genet, 1995. **29**: p. 777-807.

26. Lopes-Pacheco, M., *CFTR Modulators: Shedding Light on Precision Medicine for Cystic Fibrosis.* Front Pharmacol, 2016. **7**: p. 275.
27. Fiedorczuk, K. and J. Chen, *Molecular structures reveal synergistic rescue of Delta508 CFTR by Trikafta modulators.* Science, 2022. **378**(6617): p. 284-290.
28. Cheng, S.H., et al., *Defective intracellular transport and processing of CFTR is the molecular basis of most cystic fibrosis.* Cell, 1990. **63**(4): p. 827-34.
29. Lukacs, G.L., et al., *The delta F508 mutation decreases the stability of cystic fibrosis transmembrane conductance regulator in the plasma membrane. Determination of functional half-lives on transfected cells.* J Biol Chem, 1993. **268**(29): p. 21592-8.
30. Miki, H., et al., *Potentiation of disease-associated cystic fibrosis transmembrane conductance regulator mutants by hydrolyzable ATP analogs.* J Biol Chem, 2010. **285**(26): p. 19967-75.
31. Jih, K.Y., et al., *The most common cystic fibrosis-associated mutation destabilizes the dimeric state of the nucleotide-binding domains of CFTR.* J Physiol, 2011. **589**(Pt 11): p. 2719-31.
32. Kopeikin, Z., et al., *Combined effects of VX-770 and VX-809 on several functional abnormalities of F508del-CFTR channels.* J Cyst Fibros, 2014. **13**(5): p. 508-14.
33. Sorum, B., D. Czege, and L. Csanady, *Timing of CFTR pore opening and structure of its transition state.* Cell, 2015. **163**(3): p. 724-33.
34. Hamosh, A., et al., *Cystic fibrosis patients bearing both the common missense mutation Gly----Asp at codon 551 and the delta F508 mutation are clinically indistinguishable from delta F508 homozygotes, except for decreased risk of meconium ileus.* Am J Hum Genet, 1992. **51**(2): p. 245-50.
35. Li, C., et al., *ATPase activity of the cystic fibrosis transmembrane conductance regulator.* J Biol Chem, 1996. **271**(45): p. 28463-8.
36. Bompadre, S.G., et al., *G551D and G1349D, two CF-associated mutations in the signature sequences of CFTR, exhibit distinct gating defects.* J Gen Physiol, 2007. **129**(4): p. 285-98.
37. Lin, W.Y., K.Y. Jih, and T.C. Hwang, *A single amino acid substitution in CFTR converts ATP to an inhibitory ligand.* J Gen Physiol, 2014. **144**(4): p. 311-20.

38. Drumm, M.L., et al., *Chloride conductance expressed by delta F508 and other mutant CFTRs in Xenopus oocytes.* Science, 1991. **254**(5039): p. 1797-9.
39. Wang, F., et al., *Deletion of phenylalanine 508 causes attenuated phosphorylation-dependent activation of CFTR chloride channels.* J Physiol, 2000. **524 Pt 3**(Pt 3): p. 637-48.
40. Wilkinson, D.J., et al., *CFTR: the nucleotide binding folds regulate the accessibility and stability of the activated state.* J Gen Physiol, 1996. **107**(1): p. 103-19.
41. Cui, G., et al., *VX-770-mediated potentiation of numerous human CFTR disease mutants is influenced by phosphorylation level.* Sci Rep, 2019. **9**(1): p. 13460.
42. Wang, W., et al., *G551D mutation impairs PKA-dependent activation of CFTR channel that can be restored by novel GOF mutations.* Am J Physiol Lung Cell Mol Physiol, 2020. **319**(5): p. L770-L785.
43. Jih, K.Y. and T.C. Hwang, *Vx-770 potentiates CFTR function by promoting decoupling between the gating cycle and ATP hydrolysis cycle.* Proc Natl Acad Sci U S A, 2013. **110**(11): p. 4404-9.
44. Fiedorczuk, K. and J. Chen, *Mechanism of CFTR correction by type I folding correctors.* Cell, 2022. **185**(1): p. 158-168 e11.
45. Laselva, O., M.C. Ardelean, and C.E. Bear, *Phenotyping Rare CFTR Mutations Reveal Functional Expression Defects Restored by TRIKAFTA(TM).* J Pers Med, 2021. **11**(4).
46. Shaughnessy, C.A., P.L. Zeitlin, and P.E. Bratcher, *Elexacaftor is a CFTR potentiator and acts synergistically with ivacaftor during acute and chronic treatment.* Sci Rep, 2021. **11**(1): p. 19810.
47. Veit, G., C. Vaccarin, and G.L. Lukacs, *Elexacaftor co-potentiates the activity of F508del and gating mutants of CFTR.* J Cyst Fibros, 2021. **20**(5): p. 895-898.
48. Veit, G., et al., *Allosteric folding correction of F508del and rare CFTR mutants by elexacaftor-tezacaftor-ivacaftor (Trikafta) combination.* JCI Insight, 2020. **5**(18).
49. Balazs, A., et al., *The potentiator ivacaftor is essential for pharmacological restoration of F508del-CFTR function and mucociliary clearance in cystic fibrosis.* JCI Insight, 2025. **10**(10).

50. Keating, C., et al., *Vanzacaftor-tezacaftor-deutivacaftor versus elexacaftor-tezacaftor-ivacaftor in individuals with cystic fibrosis aged 12 years and older (SKYLINE Trials VX20-121-102 and VX20-121-103): results from two randomised, active-controlled, phase 3 trials.* Lancet Respir Med, 2025. **13**(3): p. 256-271.
51. Deák, A., et al., *A magyar Cystás Fibrosis Regiszter genetikai revíziója.* Orvosi Hetilap, 2022. **163**(51).
52. Cheng, H., et al., *Genetic analysis and intracytoplasmic sperm injection outcomes of Chinese patients with congenital bilateral absence of vas deferens.* J Assist Reprod Genet, 2022. **39**(3): p. 719-728.
53. Cuppens, H., et al., *Detection of 98.5% of the mutations in 200 Belgian cystic fibrosis alleles by reverse dot-blot and sequencing of the complete coding region and exon/intron junctions of the CFTR gene.* Genomics, 1993. **18**(3): p. 693-7.
54. des Georges, M., et al., *High heterogeneity of CFTR mutations and unexpected low incidence of cystic fibrosis in the Mediterranean France.* J Cyst Fibros, 2004. **3**(4): p. 265-72.
55. Ferec, C., et al., *Genotype analysis of adult cystic fibrosis patients.* Hum Mol Genet, 1993. **2**(10): p. 1557-60.
56. Fustik, S., et al., *Two Years of Newborn Screening for Cystic Fibrosis in North Macedonia: First Experience.* Balkan J Med Genet, 2021. **24**(1): p. 41-46.
57. Hatton, A., et al., *Reclassifying inconclusive diagnosis after newborn screening for cystic fibrosis. Moving forward.* J Cyst Fibros, 2022. **21**(3): p. 448-455.
58. Ivady, G., et al., *Analytical parameters and validation of homopolymer detection in a pyrosequencing-based next generation sequencing system.* BMC Genomics, 2018. **19**(1): p. 158.
59. Krenkova, P., et al., *Evaluation of high-resolution melting (HRM) for mutation scanning of selected exons of the CFTR gene.* Folia Biol (Praha), 2009. **55**(6): p. 238-42.
60. Ockenga, J., et al., *Mutations of the cystic fibrosis gene, but not cationic trypsinogen gene, are associated with recurrent or chronic idiopathic pancreatitis.* Am J Gastroenterol, 2000. **95**(8): p. 2061-7.

61. Sobczynska-Tomaszewska, A., et al., *Newborn screening for cystic fibrosis: Polish 4 years' experience with CFTR sequencing strategy.* Eur J Hum Genet, 2013. **21**(4): p. 391-6.
62. Wagner, K., et al., *A new missense mutation G126D in exon 4 of the cystic fibrosis transmembrane conductance regulator (CFTR) gene.* Hum Hered, 1994. **44**(1): p. 56-7.
63. Liu, S., et al., *Dynamic activation of cystic fibrosis transmembrane conductance regulator by type 3 and type 4D phosphodiesterase inhibitors.* J Pharmacol Exp Ther, 2005. **314**(2): p. 846-54.
64. Turner, M.J., et al., *The dual phosphodiesterase 3/4 inhibitor RPL554 stimulates rare class III and IV CFTR mutants.* Am J Physiol Lung Cell Mol Physiol, 2020. **318**(5): p. L908-L920.
65. de Poel, E., et al., *FDA-approved drug screening in patient-derived organoids demonstrates potential of drug repurposing for rare cystic fibrosis genotypes.* J Cyst Fibros, 2023. **22**(3): p. 548-559.
66. Rab, A., Hong, J. S., Manfredi, C., Joshi, D., Ponnaluri, S., Tracy, W. F., Luo, Y., Yang, X., and A.A. Kolykhalov, Davies, H. M. L., & Sorscher, E. J., *A novel drug series optimized to address cystic fibrosis and other CFTR deficiency diseases of human airways.* npj | drug discovery, 2025. **2**(27).
67. Csanady, L., *Rapid kinetic analysis of multichannel records by a simultaneous fit to all dwell-time histograms.* Biophys J, 2000. **78**(2): p. 785-99.
68. Zhou, Z., et al., *High affinity ATP/ADP analogues as new tools for studying CFTR gating.* J Physiol, 2005. **569**(Pt 2): p. 447-57.
69. Csanady, L., et al., *Conformational changes in the catalytically inactive nucleotide-binding site of CFTR.* J Gen Physiol, 2013. **142**(1): p. 61-73.
70. Schauble, S., et al., *Identification of ChChd3 as a novel substrate of the cAMP-dependent protein kinase (PKA) using an analog-sensitive catalytic subunit.* J Biol Chem, 2007. **282**(20): p. 14952-9.
71. Gregory, R.J., et al., *Expression and characterization of the cystic fibrosis transmembrane conductance regulator.* Nature, 1990. **347**(6291): p. 382-6.
72. Bihler, H., et al., *In vitro modulator responsiveness of 655 CFTR variants found in people with cystic fibrosis.* J Cyst Fibros, 2024.

73. Keating, D., et al., *VX-445-Tezacaftor-Ivacaftor in Patients with Cystic Fibrosis and One or Two Phe508del Alleles.* N Engl J Med, 2018. **379**(17): p. 1612-1620.
74. Pigliasco, F., et al., *Simultaneous Quantification of Ivacaftor, Tezacaftor, and Elexacaftor in Cystic Fibrosis Patients' Plasma by a Novel LC-MS/MS Method.* Biomedicines, 2023. **11**(2).
75. Ryan, K.J., et al., *Quantitation of cystic fibrosis triple combination therapy, elexacaftor/tezacaftor/ivacaftor, in human plasma and cellular lysate.* J Chromatogr B Analyt Technol Biomed Life Sci, 2022. **1213**: p. 123518.
76. Phuan, P.W., et al., *CFTR modulator therapy for cystic fibrosis caused by the rare c.3700A>G mutation.* J Cyst Fibros, 2021. **20**(3): p. 452-459.
77. Matthes, E., et al., *Low free drug concentration prevents inhibition of F508del CFTR functional expression by the potentiator VX-770 (ivacaftor).* Br J Pharmacol, 2016. **173**(3): p. 459-70.
78. Csanady, L. and B. Torocsik, *Cystic fibrosis drug ivacaftor stimulates CFTR channels at picomolar concentrations.* Elife, 2019. **8**.
79. Li, H., et al., *Two rare variants that affect the same amino acid in CFTR have distinct responses to ivacaftor.* J Physiol, 2024. **602**(2): p. 333-354.
80. Bompadre, S.G., M. Li, and T.C. Hwang, *Mechanism of G551D-CFTR (cystic fibrosis transmembrane conductance regulator) potentiation by a high affinity ATP analog.* J Biol Chem, 2008. **283**(9): p. 5364-9.
81. Yeh, H.I., et al., *Functional stability of CFTR depends on tight binding of ATP at its degenerate ATP-binding site.* J Physiol, 2021. **599**(20): p. 4625-4642.
82. Wang, C., et al., *Mechanism of dual pharmacological correction and potentiation of human CFTR*. 2022, openRxiv.
83. Hwang, T.C., et al., *Regulation of the gating of cystic fibrosis transmembrane conductance regulator C1 channels by phosphorylation and ATP hydrolysis.* Proc Natl Acad Sci U S A, 1994. **91**(11): p. 4698-702.
84. Szellas, T. and G. Nagel, *Apparent affinity of CFTR for ATP is increased by continuous kinase activity.* FEBS Lett, 2003. **535**(1-3): p. 141-6.
85. Csanady, L., et al., *Preferential phosphorylation of R-domain Serine 768 dampens activation of CFTR channels by PKA.* J Gen Physiol, 2005. **125**(2): p. 171-86.

86. Han, S.T., et al., *Residual function of cystic fibrosis mutants predicts response to small molecule CFTR modulators.* JCI Insight, 2018. **3**(14).
87. Vergani, P., A.C. Nairn, and D.C. Gadsby, *On the mechanism of MgATP-dependent gating of CFTR Cl- channels.* J Gen Physiol, 2003. **121**(1): p. 17-36.
88. Zhou, Z., et al., *The two ATP binding sites of cystic fibrosis transmembrane conductance regulator (CFTR) play distinct roles in gating kinetics and energetics.* J Gen Physiol, 2006. **128**(4): p. 413-22.
89. Sorum, B., B. Torocsik, and L. Csanady, *Asymmetry of movements in CFTR's two ATP sites during pore opening serves their distinct functions.* Elife, 2017. **6**.
90. Cutting, G.R., *Cystic fibrosis genetics: from molecular understanding to clinical application.* Nat Rev Genet, 2015. **16**(1): p. 45-56.

9. Bibliography of own publications

9.1. Publications forming the basis of the dissertation

– Závoti O, Simon MA, Csanády L. Altered functional interactions between CFTR disease mutants DeltaF508 and G551D and the protein kinase A catalytic subunit. J Physiol. 2026; 604(8):3344-3362. doi: 10.1113/JP290798.

– Závoti O, Csanády L. Molecular and pharmacological evaluation of rare, cystic fibrosis-causing missense mutations of the CFTR channel. *J Physiol*. 2025;603(19):5437-5453. doi:10.1113/JP288955

9.2. Other publications

– Voniatis C, Závoti O, Manikion K, Budavári B, Hajdu AJ. Fabrication of Mechanically Enhanced, Suturable, Fibrous Hydrogel Membranes. Membranes (Basel). 2023;13(1):116. Published 2023 Jan 16. doi:10.3390/membranes13010116

10. Acknowledgements

I would like to express my deepest gratitude to my supervisor, Dr. László Csanády, for his invaluable guidance and mentorship throughout my doctoral studies. Under his supervision, I had the opportunity to acquire both the theoretical knowledge and practical skills of ion channel electrophysiology. His continuous support, insightful discussions, and open-door attitude created an inspiring and encouraging research environment. I am especially grateful for the many opportunities he provided to attend international conferences, which greatly broadened my scientific perspective.

I would also like to thank all members of the Ion Channel Research Group for their helpfulness, constructive advice, and the stimulating atmosphere they created. In particular, I am grateful to Dr. Beáta Törőcsik, Dr. András Szöllősi, Dr. Iordan Iordanov, Dr. Ádám Bartók, Dr. Balázs Tóth, Dr. Csaba Mihályi, Dr. Márton András Simon, Ádám Tóth, Dr. Kristóf Asztalos, and Petra Lili Tóth for their support and collaboration, which have been essential to my work.

Finally, I am deeply grateful to my girlfriend and my family for their unwavering support, patience, and encouragement throughout my PhD years. Their belief in me made this journey possible.